

Magnetic response trends in cuprates and the t - t' Hubbard modelJulian Mußhoff,^{1,2} Amin Kiani,¹ and Eva Pavarini^{1,3}¹*Institute for Advanced Simulation, Forschungszentrum Jülich, 52425 Jülich, Germany*²*Department of Physics, RWTH Aachen, Germany*³*JARA High-Performance Computing, RWTH Aachen University, 52062 Aachen, Germany*

(Received 28 October 2020; revised 9 December 2020; accepted 27 January 2021; published 22 February 2021)

We perform a systematic study of static and dynamical magnetic properties of the t - t' Hubbard model in a parameter regime relevant for high-temperature superconducting cuprates. We adopt as solution method the dynamical mean-field theory approximation and its real-space cluster extension. Our results show that large t'/t suppresses incommensurate features and eventually leads to ferromagnetic instabilities for sufficiently large hole doping x . We identify isosbestic points which separate parts of the Brillouin zone with different scaling behaviors. Calculations are compared to available nuclear magnetic resonance, nuclear quadrupole resonance, inelastic neutron scattering, and resonant inelastic x-ray scattering experiments. We show that while many trends are correctly described, e.g., the evolution with x , some aspects of the spin-lattice relaxation rates can apparently only be explained invoking accidental cancellations. In order to capture the material dependence of magnetic properties in full, it may be necessary to add further degrees of freedom.

DOI: [10.1103/PhysRevB.103.075136](https://doi.org/10.1103/PhysRevB.103.075136)**I. INTRODUCTION**

High-temperature superconducting cuprates (HTSCs), a representative system of which is shown in Fig. 1, remain puzzling decades since their discovery [1–3]. Spin fluctuations have been early on suggested as possible keys to unravel the nature of superconductivity. Magnetic properties have been thus investigated via a number of different techniques, ranging from elastic and inelastic neutron scattering (INS), inelastic resonant x-ray scattering (RIXS), to magnetic susceptibility measurements, nuclear magnetic resonance (NMR), and nuclear quadrupole resonance (NQR) experiments [2–49]. Theoretical investigations have followed. They are based on a bonanza of strategies, from phenomenological approaches to *ab initio* methods based on density-functional theory to techniques for solving representative many-body models [50–64]. In the last few years, important steps forward have been made by reanalyzing the problem with state-of-the-art methods [65–81].

One of the paradigmatic—and most studied—models used for HTSCs is the single-band Hubbard Hamiltonian, assumed to describe the low-energy electronic states stemming from the CuO_2 planes, shown in Fig. 2. From the electronic structure point of view, the justification of such a model relies on the fact that the $\text{Cu } 3d x^2 - y^2$ -like band crossing the Fermi level is a generic feature of cuprates [62,63]. In addition, for magnetism, the one-band model description is grounded on the single spin-fluid scenario, which emerges from Knight shift and susceptibility measurements in $\text{YBa}_2\text{Cu}_3\text{O}_{7-\delta}$ [33,37,51]. Within the single-band Hubbard model, band-structure calculations have shown [62] that key aspects of the material dependence are captured by changes in the hopping-integral range, $r \sim t'/t$. In this picture, the actual value of the ratio t'/t is controlled by $\tilde{\epsilon}_s$, the energy of the

axial orbital [62,63]. Remarkably, many electronic properties in the doped single-band Hubbard model turned out to be very sensitive to the value of t'/t , for example the strength of antiferromagnetic correlations [61]. Recent ground-state studies of the Hubbard model based on the density-matrix renormalization group approach indicate that a finite t' might be crucial for ground-state properties, superconductivity [72,74,75], as well as for stripe order [75,76]. Furthermore, investigations of the t - t' - J model, the large- U limit of the doped Hubbard model, have identified spectroscopic signatures of t' in charge and spin dynamics of one-dimensional antiferromagnets [73].

In parallel to these successes, however, some problems came to light. The single spin-fluid picture has been challenged in $\text{La}_{2-x}\text{Sr}_x\text{CuO}_4$ and $\text{HgBa}_2\text{CuO}_{4+\delta}$ [43,44], based on recent reanalyses of NMR and NQR experiments. This, in turn, raises questions on the description of magnetic properties based on the single-band Hubbard model. The validity of the single-fluid scenario relies not only on its power of describing the qualitative picture but also on the extent to which it captures essential differences in the magnetic properties of the various families of cuprates. Despite past and present successes, as well as impressive theoretical advances [50–81], a systematic investigation of two-particle magnetic properties in this direction, to the best of our knowledge, is still missing. It is thus time to reanalyze the problem. The purpose of the present work is to fill holes in this contest.

To this end, we calculate the evolution of static and dynamical magnetic response with the number x of holes in the CuO_2 plane, from the underdoped all the way to the less explored highly overdoped regime, progressively increasing t'/t and the strength of the Coulomb interaction U . We employ as a method the single-site and the cluster dynamical mean-field theory (DMFT) approach, adopting quantum Monte Carlo

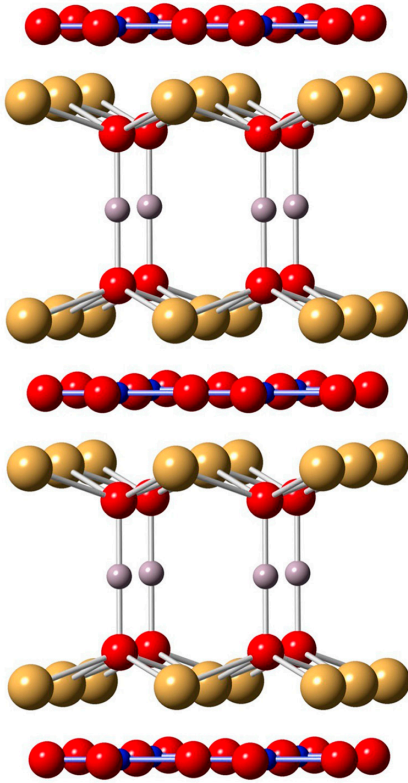


FIG. 1. The crystal structure of the single-layered high-temperature superconducting cuprate $\text{HgBa}_2\text{CuO}_4$. Three CuO_2 planes (described in more detail in Fig. 2) are shown.

(QMC) impurity solvers. The results obtained show that progressively increasing t' and x suppresses antiferromagnetism, favoring first incommensurate instabilities around the M point and eventually ferromagnetic correlations. We find that the nature of magnetic correlations changes very strongly entering the overdoped regime. We identify isosbestic points which separate regions of the Brillouin zone with different scaling behaviors. We show that the magnetic trends do not change qualitatively with increasing U , provided that one stays away from the $U \ll U_c$ regime, where U_c is the critical value for the Mott transition at half filling; a large U makes however ferromagnetic instabilities more likely in the overdoped regime. We show that while many aspects of the experimental doping dependence, for example uniform susceptibility and Knight shift measurements or the resonance mode in the underdoped regime, are well captured, others are not—in particular concerning experimental NMR and NQR spin-lattice relaxation rates. For the realistic description of such properties it might be necessary to go beyond the simple t - t' Hubbard model.

The paper is organized as follows. In Sec. II, we present the method employed. In Sec. III we present the results, first for the static and then the dynamical magnetic properties. Finally we give our conclusions in Sec. IV. Additional technical details can be found in Appendices A and B.

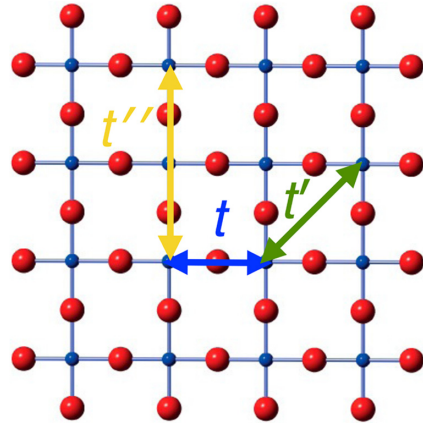


FIG. 2. The CuO_2 plane in the middle of Fig. 1. Cu: Small spheres; O: large spheres. The hopping integrals t , t' , t'' of the single-band Hubbard model are also shown.

II. MODEL AND METHOD

We describe the low-lying states via the single-band Hubbard model

$$H = - \sum_{i i' \sigma} t^{i, i'} c_{i\sigma}^\dagger c_{i'\sigma} + U \sum_i n_{i\uparrow} n_{i\downarrow}. \quad (1)$$

Here $c_{i\sigma}^\dagger$ ($c_{i\sigma}$) creates (annihilates) an electron at site i with spin σ and $n_i = c_{i\sigma}^\dagger c_{i\sigma}$, and U is the screened Coulomb interaction. The parameter $t^{i, i'}$ is the hopping integral between sites i and i' . For high-temperature superconducting cuprates (see Fig. 2) the key terms are the nearest-neighbor and next-nearest-neighbor hopping integrals, t and $-t'$. This leads to the band dispersion $\varepsilon(\mathbf{k}) = -2t(\cos k_x + \cos k_y) + 4t' \cos k_x \cos k_y$. It has been previously established [62] that realistic values are $t \sim 0.4$ eV, with t'/t ranging from $t'/t \sim 0.17$ for $\text{La}_{2-x}\text{Sr}_x\text{CuO}_4$ to $t'/t \sim 0.33$ for $\text{YBa}_2\text{Cu}_3\text{O}_{7-\delta}$ or $\text{HgBa}_2\text{CuO}_{4+\delta}$. Here we thus study the magnetic properties for t'/t in the range $0 \leq t'/t < 0.4$, for hole-doping corresponding to $0 < x < 0.4$. This covers the full range from underdoped to the heavily overdoped regime and well beyond; optimal doping is around $x \sim 0.16$ in many cuprate families [3]. More controversial is the estimate of the screened Coulomb repulsion. Spin-wave measurements could be taken as evidence of a relatively weak direct (screened) Coulomb interaction, $U \sim 3$ eV; this is due to the fact that the behavior of the experimental spin-wave dispersion appears not compatible with the antiferromagnetic J_1 - J_2 Heisenberg model derived from the Hubbard model in second-order perturbation theory. Its description requires [5] either a ferromagnetic (negative) value of J_2 or higher-order interactions, for example a ring-type four-spin superexchange term [82,83], negligible in the very large U limit. A relatively small U is also supported by constrained random-phase approximation (cRPA) calculations [84,85]. On the other hand, a small ferromagnetic J_2 can arise from the standard ferromagnetic intersite Coulomb exchange coupling and/or multiorbital superexchange effects. Indeed, ferromagnetic couplings $J_2 \sim -10$ meV, sufficiently large, have been obtained theoretically using a first-principles linear-response approach [54]. Furthermore, cRPA calculations often overestimate screening effects. Much larger values

of U , up to 10 eV, have been estimated via the constrained local-density approximation (cLDA) approach [86–89]. This technique, on the other hand, tends to overestimate the Coulomb repulsion, in part due to the fact the more localized functions are typically used as basis, in part because fewer screening channels are considered [89]. Taking all this into consideration, in this paper we present results for several values of U in the interval between the cRPA and cLDA estimates and discuss the most important effects of increasing U for magnetism.

We solve the Hamiltonian (1) via the dynamical mean-field theory (DMFT) and its real-space cluster extension (cDMFT) [64,90–92]. In this context, some additional remarks on the choice of the screened Coulomb parameter are in place. Within paramagnetic dynamical mean-field theory, a small U is hard to conciliate with a relatively large experimental [93–96] gap of ~ 2 eV. More specifically, for the hopping parameters used in this work, the critical U for the metal-insulator transition is about $U_c \sim 4.5$ eV. Since a consistent picture of the whole phase diagram cannot be fully recovered if $U < U_c$, we first systematically explore the case $U \sim 7$ eV. This value yields at half filling a gap ~ 2 eV in paramagnetic DMFT calculations, i.e., a gap in line with photoemission spectroscopy [93], photoinduced absorption spectroscopy [94], and optical conductivity measurements [95], as well as with the reported observation of upper Hubbard bands [3,96]. Next we study the effects of varying U in the range from 3 to 11 eV, all values adopted in the literature. DMFT is exact in the infinite-ordination limit, in which the self-energy is momentum independent. In the case of the t - t' Hubbard model it is therefore an approximation. For magnetic properties, nonlocal effects become important in particular approaching a phase transition [97]. Thus, in the most relevant cases we compare DMFT results with those of 2- and 4-site cellular DMFT (cDMFT) calculations, which have been shown to capture key effects of spatial fluctuations [78,98].

For the quantum impurity solvers we chose two similar but complementary approaches. The first is the Hirsch-Fye (HF) quantum Monte Carlo (QMC) method [99], in the implementation presented in Ref. [100]. The second is the hybridization-expansion continuous-time QMC method (CT-HYB) [101], in the implementation of Refs. [102,103]. The bottleneck, in both approaches, is the calculation of the local susceptibility tensor [92], which is performed at the end of the self-consistency DMFT loop. This is defined as

$$\chi^\alpha(\boldsymbol{\tau}) = \langle \mathcal{T} c_{\alpha_1}(\tau_1) c_{\alpha_2}^\dagger(\tau_2) c_{\alpha_3}(\tau_3) c_{\alpha_4}^\dagger(\tau_4) \rangle - \langle \mathcal{T} c_{\alpha_1}(\tau_1) c_{\alpha_2}^\dagger(\tau_2) \rangle \langle \mathcal{T} c_{\alpha_3}(\tau_3) c_{\alpha_4}^\dagger(\tau_4) \rangle. \quad (2)$$

Here \mathcal{T} is the time order operator, $\boldsymbol{\tau} = (\tau_1, \tau_2, \tau_3, \tau_4)$ are the imaginary times; $\boldsymbol{\alpha} = (\alpha_1, \alpha_2, \alpha_3, \alpha_4)$ and $\alpha_j = m_j \sigma_j i_j$ are collective orbital (m_j), spin (σ_j), and site (i_j). The calculation is performed in different ways, depending on the solver. In Hirsch-Fye QMC simulations we compute it directly in Matsubara frequency space. This yields $\chi^\alpha(\boldsymbol{\nu})$, where $\boldsymbol{\nu} = (v_n, -v_n - \omega_m, v_{n'} + \omega_m, -v_{n'})$, v_n and $v_{n'}$ are fermionic and ω_m bosonic Matsubara frequencies, the Fourier transform of $\chi^\alpha(\boldsymbol{\tau})$. To reduce the computational time we obtain the Fourier transform of the Green's function matrix $G_{\alpha,\alpha'}(\tau, \tau')$ by shifting the discontinuity at $\tau = \tau'$ to the border, and

apply the semianalytical Filon-trapezoidal approach [100]. In the CT-HYB QMC solver we perform the calculations in compact polynomial representations (Legendre and numerical polynomial basis); when necessary we transform to the Matsubara frequency representation. More details on the approach adopted in our general implementation can be found in Refs. [102,103].

Next we use the (c)DMFT lattice Green's function $G_{\alpha_i \alpha_j}(\mathbf{k}; i\nu_n)$, obtained from the noninteracting Hamiltonian and the (c)DMFT self-energy, and compute the bubble contribution to the lattice and local susceptibility. They are defined respectively via the tensors

$$\chi_0^\alpha(\mathbf{q}; i\omega_m) = -\beta \delta_{nn'} \delta_{\sigma_2 \sigma_3} \delta_{\sigma_1 \sigma_4} \frac{1}{N_{\mathbf{k}}} \times \sum_{\mathbf{k}} G_{\alpha_3 \alpha_2}(\mathbf{k} + \mathbf{q}; i\nu_n + i\omega_m) G_{\alpha_1 \alpha_4}(\mathbf{k}; i\nu_n), \quad (3)$$

where $\beta = 1/T$ is the inverse temperature and

$$\chi_0^\alpha(i\omega_m) = \frac{1}{N_{\mathbf{q}}} \sum_{\mathbf{q}} \chi_0^\alpha(\mathbf{q}; i\omega_m). \quad (4)$$

The associated bubble longitudinal lattice magnetic susceptibility is given by

$$\chi_0(\mathbf{q}; i\omega_m) = \frac{(g\mu_B)^2}{4} \sum_{\alpha} (-1)^{\sigma_1 + \sigma_3} \delta_{\sigma_1 \sigma_2} \chi_0^\alpha(\mathbf{q}; i\omega_m) \delta_{\sigma_3 \sigma_4}, \quad (5)$$

where $\sigma_j = \pm 1$ for spins \uparrow and \downarrow , respectively. From the tensors given in Eq. (3) we build square matrices, e.g., $\chi^\alpha(i\omega_m) = [\chi(i\omega_m)]_{NN'}$ with elements $N = \alpha_1 n, \alpha_2 n, N' = \alpha_3 n', \alpha_4 n'$, so that for the magnetic susceptibility only the terms $\sigma_1 = \sigma_2 = \sigma$ and $\sigma_3 = \sigma_4 = \sigma'$ are taken into account [100]. In this case, the (bare) local susceptibility is zero everywhere except for the impurity block, i.e., $i_j = i_1$ for DMFT and $i_j = \{i_c\}$ for cluster DMFT calculations. In the last step, we obtain the lattice susceptibility $\chi(\mathbf{q}; i\omega_m)$ solving the Bethe-Salpeter equation in the local-vertex approximation [90,104]

$$[\chi(\mathbf{q}; i\omega_m)]^{-1} \approx [\chi_0(\mathbf{q}; i\omega_m)]^{-1} - \Gamma(i\omega_m). \quad (6)$$

The local vertex itself is given by

$$\Gamma(i\omega_m) = [\chi_0(i\omega_m)]^{-1} - [\chi(i\omega_m)]^{-1}, \quad (7)$$

where $\chi(i\omega_m)$ is the local susceptibility tensor obtained from QMC simulations. Finally, the full longitudinal lattice magnetic susceptibility is obtained as

$$\chi(\mathbf{q}; i\omega_m) = \frac{(g\mu_B)^2}{4} \sum_{\alpha} (-1)^{\sigma_1 + \sigma_3} \delta_{\sigma_1 \sigma_2} \chi^\alpha(\mathbf{q}; i\omega_m) \delta_{\sigma_3 \sigma_4}. \quad (8)$$

In the hybridization-expansion continuous-time QMC approach the Bethe-Salpeter equation is solved in the compact polynomial representation (l, l') instead of in the Matsubara fermionic frequencies (n, n') representation [103]. The Hirsch-Fye approach is better suited in the weak-interaction and large-cluster cDMFT regime, while the continuous-time solver yields the $\Delta\tau = \beta/L \rightarrow 0$ limit and it is best suited

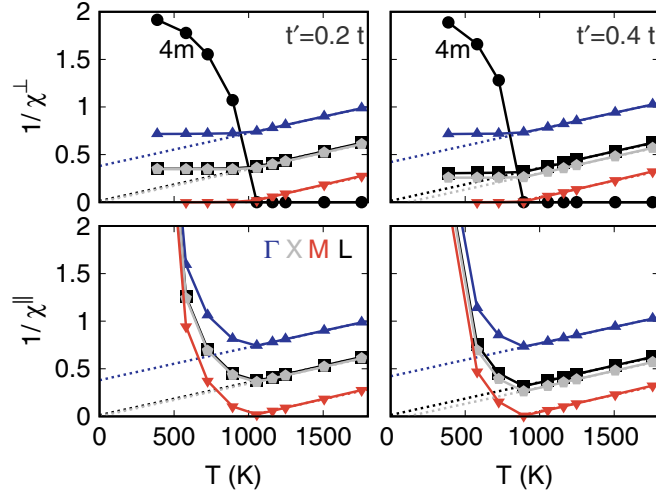


FIG. 3. Static inverse transverse and longitudinal susceptibility $\chi(\mathbf{q}; 0)$ as a function of temperature, $U = 7$ eV. Left panels: $t' = 0.2t$. Right panels: $t' = 0.4t$. Triangles: Γ and M points. Gray pentagons: X point. Black circles: Local (indicated with L in the plot) susceptibility. Above the critical temperature it shows the Curie-Weiss behavior. Dotted lines: Curie-Weiss fit at high temperature, and associated low-temperature extrapolation [97]. Black circles: $4m$, where m is the magnetization per site. Special points: $\Gamma = (0, 0, 0)$, $X = (\pi, 0, 0)$, $M = (\pi, \pi, 0)$.

for dynamical response calculations. By combining the two approaches we can study in detail different aspects of the problem. Finally, data on the real axis are obtained via analytic continuation using the maximum-entropy approach.

III. RESULTS

A. Static susceptibility for $x = 0$

We start by analyzing the lattice spin susceptibility at half filling ($x = 0$), in both the paramagnetic and antiferromagnetic phases. This sets the stage for analyzing in the next sections the finite- x case. The principal results are collected in Figs. 3, 4 and 5. In the paramagnetic phase ($T > T_N$), the DMFT static susceptibility has a Curie-Weiss-like behavior [64] in all considered cases, reflecting the mean-field approximation. This is shown in Fig. 3 for representative \mathbf{q} values. The figure also shows the transition to the antiferromagnetic phase at the critical temperature T_N . The calculations yield the (expected) mean-field behavior of the transverse and longitudinal susceptibility, with $\chi^\perp(\mathbf{q}; 0)$ going to zero in the $T \rightarrow 0$ limit and $\chi^\parallel(\mathbf{q}; 0)$ remaining constant below T_N ; here \parallel and \perp indicate the direction of the applied magnetic field with respect to the ordered magnetic moments. The temperature dependence is mostly determined by the local vertex $\Gamma(i\omega_n)$. As we have previously shown, e.g., in Ref. [100] for layered vanadates, in the paramagnetic insulating phase, the “bubble” term of the static lattice susceptibility at half filling is approximately

$$\chi_0(\mathbf{q}; 0) \approx \frac{(g\mu_B\mu_{\text{eff}})^2}{U r_0} \left\{ 1 - \frac{1}{2U} \left[J_{r_0}(\mathbf{0}) + \frac{1}{2} J_{r_0}(\mathbf{q}) \right] + \dots \right\}. \quad (9)$$

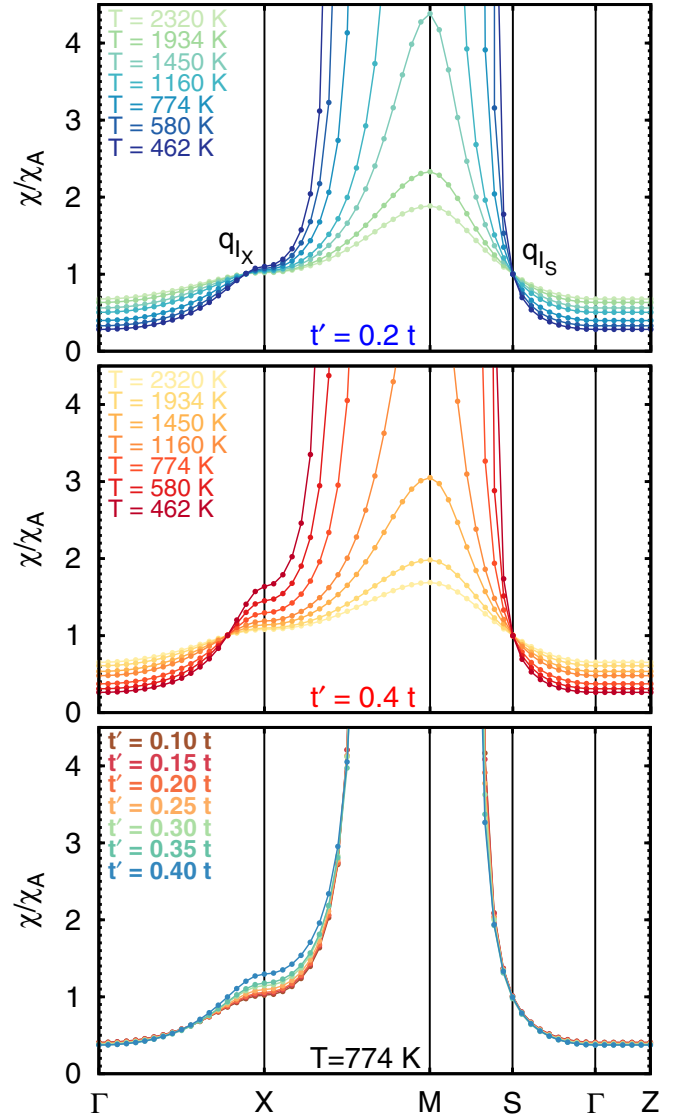


FIG. 4. Static lattice magnetic susceptibility $\chi(\mathbf{q}; 0)$ along high-symmetry lines of the Brillouin zone, normalized to the atomic susceptibility $\chi_A \sim 1/4k_B T$. Special points: $M = (\pi, \pi, 0)$, $S = (\pi/2, \pi/2, 0)$, $X = (\pi, 0, 0)$, $Z = (0, 0, \pi)$. Top: $t' \sim 0.2t$. Center: $t' \sim 0.4t$. Bottom: Results at fixed temperature, but for different values of t'/t .

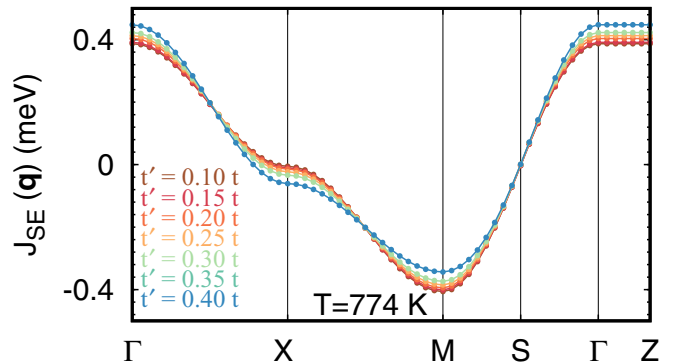


FIG. 5. Effective superexchange couplings for the susceptibilities shown in the bottom panel of Fig. 4. Special points: $M = (\pi, \pi, 0)$, $S = (\pi/2, \pi/2, 0)$, $X = (\pi, 0, 0)$, $Z = (0, 0, \pi)$.

In this equation the effective magnetic moment is defined as $\mu_{\text{eff}} = \sqrt{S(S+1)}/3$ and the value $S \sim 1/2$ is obtained independently via the equal-time correlation function (see Appendix A). The effective superexchange (SE) couplings can be obtained from the inverse of the susceptibility as follows:

$$J_{r_0}(\mathbf{q}) = ([\chi(\mathbf{q}; 0)]^{-1} - [\chi(0)]^{-1})(g\mu_B)^2 = J_{\text{SE}}(\mathbf{q})/2r_0^2, \quad (10)$$

where r_0 is a renormalization parameter and where the Fourier decomposition reads

$$J_{\text{SE}}(\mathbf{q}) \approx 2J_1(\cos q_x + \cos q_y) + 4J_2 \cos q_x \cos q_y + \dots \quad (11)$$

In the very small t/U limit, the superexchange parameters take the second-order expression $J_1 \sim J_1^{(2)} = 4t^2/U$ and $J_2 \sim J_2^{(2)} = 4t^2/U$. Increasing the ratio t/U , higher-order terms, e.g., those arising from the ring exchange coupling, J_r , can contribute [82,83]. For clarity, let us discuss explicitly the numbers in some cases. For $U = 7$ eV we have $J_1^{(2)} \sim 4t^2/U \sim 91$ meV. In this situation the 4th order term $J_{1r} = 24t^4/U^3 \sim 1.8$ meV is negligible in comparison; $J_{2r} = 4t^4/U^3$ is also small with respect to $J_2^{(2)} \sim 4$ meV ($t' = 0.2t$). The 4th order terms start to become relevant for $U \sim U_c$ and smaller, i.e., in the same regime in which charge fluctuations and double occupancies start to increase in addition. For $U \sim U_c \sim 4.5$ eV, we have $J_1^{(2)} \sim 142$ meV and $J_{1r} \sim 6.7$ meV, while $J_2^{(2)} \sim 5.7$ meV and $J_{2r} \sim 1.1$ meV. Experimental estimates of the J_1 and J_2 parameters have been obtained by fitting inelastic neutron scattering results [5,11] and magnetic susceptibility [105] or Raman scattering data [106–109]. The second-order perturbation theory value $J_1^{(2)} \sim 91$ meV ($U = 7$ eV) is slightly smaller than typical experimental estimates, while $J_1^{(2)} \sim 142$ ($U = 4.5$ eV) is slightly larger than the value for La_2CuO_4 [5]. Finally, we find that the scaling factor has values from $r_0 \sim 0.9$ to $r_0 \sim 1.0$ in the complete range of parameters considered here.

Including the local DMFT vertex we obtain (see Appendix A for a simple derivation) the static mean-field expression [64,100]

$$\chi(\mathbf{q}; 0) \approx \frac{(g\mu_B)^2 \mu_{\text{eff}}^2}{k_B T + \mu_{\text{eff}}^2 J_{\text{SE}}(\mathbf{q})}. \quad (12)$$

This approximate formula well describes our numerical data, shown in Figs. 3 and 4. On lowering the temperature, we find a divergency at the M point, the signature of an instability toward antiferromagnetism, as expected in this regime [4,7,16]. This can be seen in both Figs. 3 and 4. The figures show that we are well inside the Heisenberg-model limit of the Hubbard Hamiltonian; in this situation increasing t'/t enhances frustration, hence reduces the dynamical mean-field critical temperature T_N . The effective degree of frustration $f = J_2/J_1$ can be extracted from the susceptibility via the expression [100]

$$f \approx \frac{1}{2} \times \frac{\chi(0, \pi; 0)^{-1} - \chi(\pi/2, \pi/2; 0)^{-1}}{\chi(\pi/2, \pi/2; 0)^{-1} - \chi(\pi/2, 0; 0)^{-1}}. \quad (13)$$

For $U = 7$ eV we find that $f \sim 0.036$ for $t' = 0.2t$ and $f \sim 0.157$ for $t' = 0.4t$; hence in all cases the system remains

in the weak frustration regime, with f close to the value obtained in second-order perturbation theory, indicating that charge fluctuations and higher-order processes such as the ring-exchange are not yet playing a crucial role. In addition we find that f is weakly temperature dependent. Remarkably, we find that the qualitative behavior of the static susceptibility and the effective frustration degree change little if we reduce U from 7 eV to 4.7 eV, i.e., approaching the metal-insulator transition.

Going back to Fig. 4, at the nodal point, $S = (\pi/2, \pi/2)$, located in the middle of the ΓM line, the susceptibility is close to the atomic value, $\chi(S; 0) \sim (g\mu_B)^2 \mu_{\text{eff}}^2 / T \sim \chi_A$, since the effective superexchange coupling $J_{\text{SE}}(\mathbf{q} = S)$ is basically zero. Instead, at the antinodal points, $X = (\pi, 0)$ and $Y = (0, \pi)$, the susceptibility is close to but slightly differs from χ_A , since the term proportional to J_1 in the Fourier series $J_{\text{SE}}(\mathbf{q})$ does not contribute; thus, the susceptibility depends in first approximation only on t' (and not on t) at these \mathbf{q} vectors. Such a t' dependence is shown in detail in the bottom panel of Fig. 4 for a representative temperature. In addition, since at the X point the J_2 term is not frustrated, the susceptibility increases with lowering the temperature. As a consequence, the ratio χ/χ_A exhibits temperature-independent isosbestic points [110], e.g., one at $\mathbf{q}_S = S$ and one at a vector \mathbf{q}_X close to X along the Γ - X direction (and symmetry-equivalent \mathbf{q} vectors). This can be seen in the upper panels of Fig. 4. At the isosbestic points the susceptibility is close to the atomic limit χ_A . The exact position of \mathbf{q}_X depends on t' , so that the distance between S and \mathbf{q}_X increases with increasing t'/t ; for $t' = 0$, $\mathbf{q}_X = X$. This may be seen comparing the top and middle panels of the figure. Finally, at $(\pi/2, q_x)$ and $(q_y, \pi/2)$ the magnetic susceptibility is not influenced by t' , since $J_{\text{SE}}(\mathbf{q})$ in first approximation depends only on the term proportional to J_1 at such a \mathbf{q} vector. This in turn gives rise to isosbestic points as a function of t' at $q_x = \pi/2$ and $q_y = \pi/2$. In the bottom panel of Fig. 4 they are hard to see, but they can be seen clearly in Fig. 5, which shows the associated effective superexchange coupling, extracted via Eq. (12).

B. Dynamical susceptibility for $x = 0$

Let us now switch to the antiferromagnetic phase [97], i.e., $T < T_N$. Below the transition the static susceptibility splits into transverse and longitudinal components, as shown in Fig. 3. While the static transverse susceptibility is temperature independent, the longitudinal goes to zero in the $T \rightarrow 0$ limit. In Fig. 6 we show the spin-wave dispersion, obtained from the static susceptibility, well below the magnetic transition temperature, i.e., in the regime in which the order parameter is close to the saturation value $m \sim 1/2$. The figure shows that dynamical mean-field theory calculations basically yield the Holstein-Primakoff spin-wave dispersion for the J_2 - J_1 Heisenberg model in the small-frustration limit. This can be understood as follows. In the insulating antiferromagnetic phase the DMFT local self-energy is in first approximation close to the Hartree-Fock shift; i.e., it takes the form $\Sigma_\sigma(\omega_n) \approx -\mu + p_i U m$, where m is the magnetization; the shift changes sign ($p_i = \pm$) for neighboring sites i . In this approximation, at sufficiently low temperature and at linear

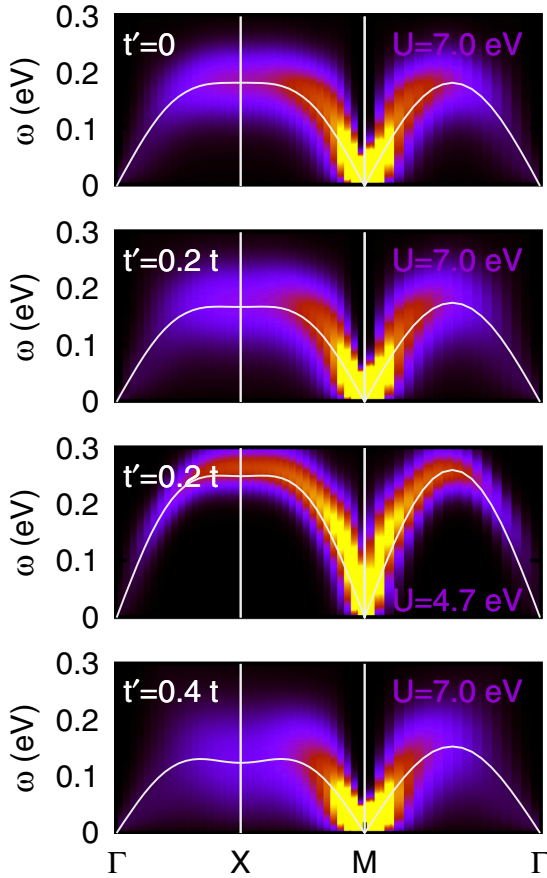


FIG. 6. Spin-wave spectra (in eV) for fixed t and for representative values of t' . The spectra are obtained from the transverse dynamical susceptibility calculated with the dynamical mean-field theory approach (intensity maps) and standard Holstein-Primakoff spin-wave theory calculated using the superexchange parameters from second-order perturbation theory (white lines). The high-symmetry points are $\Gamma = (0, 0)$, $X = (\pi, 0)$, and $M = (\pi, \pi)$.

order in J_1 , one can show (see Appendix B) that

$$\left[\frac{1}{\chi^0(\mathbf{q}; i\omega_m)} - \frac{1}{\chi^0(i\omega_m)} \right]_{\sigma-\sigma-\sigma\sigma}^{i\nu} \approx 2J_1 f_{\mathbf{q}} (1 - \delta_{i\nu}), \quad (14)$$

where $f_{\mathbf{q}} = (\cos q_x + \cos q_y)/2$. Solving the associated Bethe-Salpeter equation we have

$$\chi^\perp(\mathbf{q}; i\omega_m) \sim (g\mu_B)^2 \frac{J_1(1 - f_{\mathbf{q}})}{\omega_m^2 + 4J_1^2(1 - f_{\mathbf{q}}^2)}, \quad (15)$$

which yields the conventional spin-wave dispersion. The magnon bandwidth for $U \sim 4.7$ eV and $t' = 0.2t$ is in reasonably good agreement with the experimental results of Ref. [5] for La_2CuO_4 . The smaller experimental magnon bandwidth [12] reported in $\text{YBa}_2\text{Cu}_3\text{O}_{6.15}$ is in line with the calculation for larger t' , taking into account that the interlayer coupling is neglected here.

Summarizing, at half filling, in all ranges of parameters considered, the DMFT static susceptibility is close to the one that can be obtained from the associated Heisenberg model in the small- t/U limit. In addition, the DMFT spin-wave spectrum is very close to the corresponding expression for

conventional spin-wave theory in the weak-frustration regime. Remarkably, this remains true also for U values very close to the metal-insulator transition, as can be seen in Fig. 6, although deviations start to appear. Neutron scattering data at half filling are sufficiently well described for $U \sim 4$ to 5 eV; increasing U up to 7 eV does not alter the qualitative behavior, but merely reduces the spin-wave dispersion in an almost uniform way, only slightly modifying the effective frustration parameter f . In addition, the effect of high-order couplings and charge fluctuations remains small even for $U \sim 4.7$ eV. The main effect of reducing U is that the spin-wave bandwidth is larger due to the smaller excitation energy for charge fluctuations. The spin-wave energy at X is as high as at $S = (\pi/2, \pi/2)$, as Fig. 6 shows, indicating that high-order terms such as the ring-exchange correction are not sufficiently large for explaining experimental findings alone; a ferromagnetic term, e.g., from Coulomb exchange, would still be required for a realistic description. Instead, a larger t' is compatible with a smaller spin-wave dispersion going from La_2CuO_4 to $\text{YBa}_2\text{Cu}_3\text{O}_{6.15}$. So far, although not all details are captured, the trends are correctly described.

C. Uniform and local susceptibility for $x > 0$

Let us now analyze the results in the doped Mott insulating phase. For $x \sim 0$, when the metallic contribution is still negligible (two-pole approximation for the self-energy), the DMFT static lattice magnetic susceptibility is approximately (Appendix A) given by the Curie-Weiss-like form

$$\chi(\mathbf{q}; 0) \approx \frac{(g\mu_B\mu_{\text{eff}})^2(1-x)}{T + \mu_{\text{eff}}^2(1-x)J_{\text{SE}}(\mathbf{q})}. \quad (16)$$

In this regime the dominant spin-spin correlations remain antiferromagnetic, albeit with square local moments reduced to $\sim \mu_{\text{eff}}^2(1-x)$; this is due to the fact that double occupancies remain much smaller than in the uncorrelated limit, $\langle n_{i\uparrow}n_{i\downarrow} \rangle = 0.25(1-x)^2$, which would yield $\langle S_z^i S_z^j \rangle \sim \mu_{\text{eff}}^2(1-x^2)/2$ instead.

For small but finite x , the behavior of the uniform susceptibility deviates very quickly from Eq. (16), however. Still, the temperature dependence remains similar, $\chi(\mathbf{q}; 0) \propto 1/[T + J_{\text{eff}}(\mathbf{q})]^\alpha$, with $\alpha \sim 1$ for x not too large. We find that, while the effective local magnetic moment decreases linearly even for x as large as 0.4, the bubble term $\chi_0(\mathbf{0}; 0)$ increases with x due to the growing relevance of the metallic contribution. The result of the competition between opposite effects is the nonmonotonic behavior of $\chi(\mathbf{0}; 0)$ shown in Fig. 7. The left panels of the figure show that at a given (sufficiently low) temperature, $\chi(\mathbf{0}; 0)$ first increases, a maximum is reached at $x_c \sim 0.25$ for $t' \sim 0.2t$, and then $\chi(\mathbf{0}; 0)$ decreases. In the right panel of Fig. 7, we show how x_c increases with t'/t , going from $x_c = 0.15$ for $t' = 0.1t$ to $x_c = 0.4$ for $t' = 0.35t$; for larger $t' = 0.4t$ the magnetic susceptibility diverges at $x = 0.30$.

For $\text{La}_{2-x}\text{Sr}_x\text{CuO}_4$, characterized by $t' \sim 0.2t$, this behavior is in very good agreement with reported magnetic susceptibility [47,48] measurements—including the value of the turning point x_c . NMR Knight shift measurements [27–29,34] also show an increase with increasing x ; unfortunately, the $x > x_c$ regime was not systematically explored,

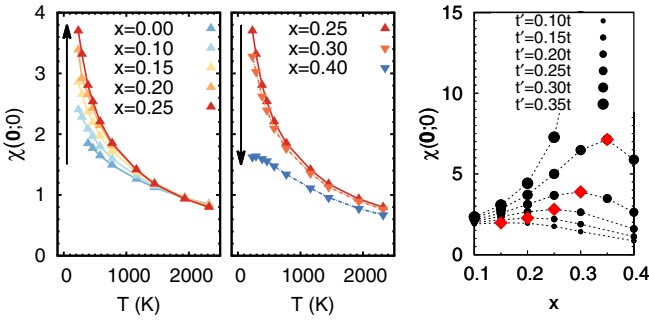


FIG. 7. Left: Static uniform magnetic susceptibility $\chi(\mathbf{0};0)$ for $t' = 0.2t$ and several values of x , as a function of the temperature, for temperatures above the pseudogap regime. The susceptibility increases with x up to $x_c \sim 0.25$ (first panel); for $x > x_c$, $\chi(\mathbf{0};0)$ it decreases (second panel). Right: $\chi(\mathbf{0};0)$ as a function of x for several values of t' , at fixed temperature, $T \sim 387$ K. The maximum is at x_c (diamonds), whose value increases with t' .

however. For $\text{YBa}_2\text{Cu}_3\text{O}_{6+y}$ an increase of Knight shifts with hole doping up to $y \sim 1$ (slightly overdoped regime) has also been reported [35–39]. Similar trends appear in $\text{HgBa}_2\text{CuO}_{4-\delta}$ [111]. In $\text{Tl}_2\text{Ba}_2\text{CuO}_{6+y}$ [34,40,41], which is considered to be heavily overdoped, the opposite behavior is observed, as one would indeed expect in the present description decreasing x while starting from $x > x_c$. While further systematic experiments would help in clarifying this point, the description based on the t - t' Hubbard model appears therefore to capture the trends in the observations so far.

One important conclusion is that the nonmonotonic x dependence is specific of the Γ point and the \mathbf{q} vectors around it. The local susceptibility, the average over the \mathbf{q} vectors, merely decreases with x going from $x = 0$ to $x = 0.4$. This is shown in Fig. 8. The figure compares, in addition, single-site calculations ($\chi_{1\text{SC}}$) with 2- and 4-site cluster results ($\chi_{2\text{SC}}$, $\chi_{4\text{SC}}$) and shows that differences are minor. At a fixed temperature, for a given t' , we find $\chi_{1\text{SC}} > \chi_{2\text{SC}} > \chi_{4\text{SC}}$ if x is sufficiently small, while the opposite is true ($\chi_{1\text{SC}} < \chi_{2\text{SC}} < \chi_{4\text{SC}}$) for large x . The same reversal is found for x fixed and t' increasing. The effect remains however very small, as the figure shows; picture and trend remain unchanged. The static local susceptibility, in the temperature regime analyzed, scales to a very good approximation as

$$\chi(0) \sim \frac{(g\mu_B)^2 \mu_{\text{eff}}^2 (1-x)}{T + T_0(x)}, \quad (17)$$

where $T_0(x)$ increases with increasing x and decreases with increasing t' . More specifically, $T_0(x) \sim 16$ K for $x = 0$ and $t' = 0.2t$; keeping t'/t fixed and increasing x , $T_0(x) \sim 200$ K for $x = 0.1$ and $T_0(x) \sim 920$ K for $x = 0.4$. For $t' = 0.4t$ the corresponding values are $T_0(x) \sim 6$ K for $x = 0$, $T_0(x) \sim 190$ K for $x = 0.1$, and $T_0(x) \sim 630$ K for $x = 0.4$. We emphasize once more that the scaling with x is very different for local and uniform susceptibility. Extracting the analogue of $T_0(x)$ at $\mathbf{q} = 0$ with a similar procedure would yield a characteristic scale first decreasing ($x < x_c$) and then ($x > x_c$) increasing with x . For $x < 0.2$ such a scaling has been indeed identified early on from analysis of uniform susceptibility measurements [49].

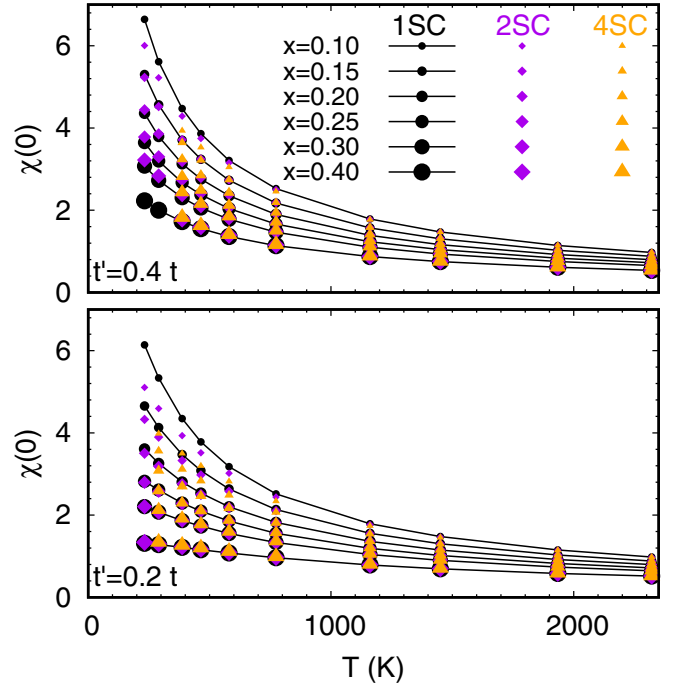


FIG. 8. Static local magnetic susceptibility for $t' = 0.2t$ (top) and $t' = 0.4t$ (bottom) as a function of temperature and for several x values from single-site DMFT, two- and four-site CDMFT calculations (labeled as 1SC, 2SC, and 4SC in the caption).

D. Static $x > 0$ susceptibility: \mathbf{q} dependence

Let us now analyze in detail the entire \mathbf{q} dependence. Figure 9 collects the most important results. The top panels show the case $t' = 0.2t$. In the figure the value of x increases from $x = 0.1$ to $x = 0.4$ going from left to right. The first two panels on the left show underdoped and slightly underdoped regimes, $x \sim 0.10$ and $x \sim 0.15$. For $x = 0.10$ the expected dominant instability is antiferromagnetic, as in the half-filling or $x = 0$ limit, and the susceptibility is still not far from the Curie-Weiss-like form, although with reduced local moments. Around $x = 0.15$ the picture changes, however. For $T < 460$ K peaks at incommensurate vectors appear. This can be seen in Fig. 9, second top panels from the left. There are two types of potential instabilities, the one at \mathbf{q}_{XM} , a vector close to M along the XM direction, and the one at $\mathbf{q}_{\Gamma M}$, a vector close to M along the ΓM high-symmetry line. The associated critical temperatures $T_C(\mathbf{q}_{\Gamma M})$ and $T_C(\mathbf{q}_{XM})$, obtained via linear extrapolation from the inverse susceptibility, are both of the order of $\sim T_N/10$, where $T_N = T_C(M)$ for $x = 0$. It is important to point out that the mean-field critical temperatures just discussed are excellent estimates of the actual strength of the effective magnetic coupling $J_{\text{eff}}(\mathbf{q})$, as Eq. (16), Fig. 5, and the surrounding discussion illustrate.

The trends thus suggest that in the ground state static incommensurate structures could be realized in this regime. Further increasing x progressively suppresses the magnetic response around the M point, giving rise to a depression in M . This can be seen moving from left to right in Fig. 9, top panels. It can be noticed that the reduction of the magnetic response is not uniform in \mathbf{q} and x . At the Γ point, as we have already discussed, for $t' = 0.2t$ the susceptibility at first

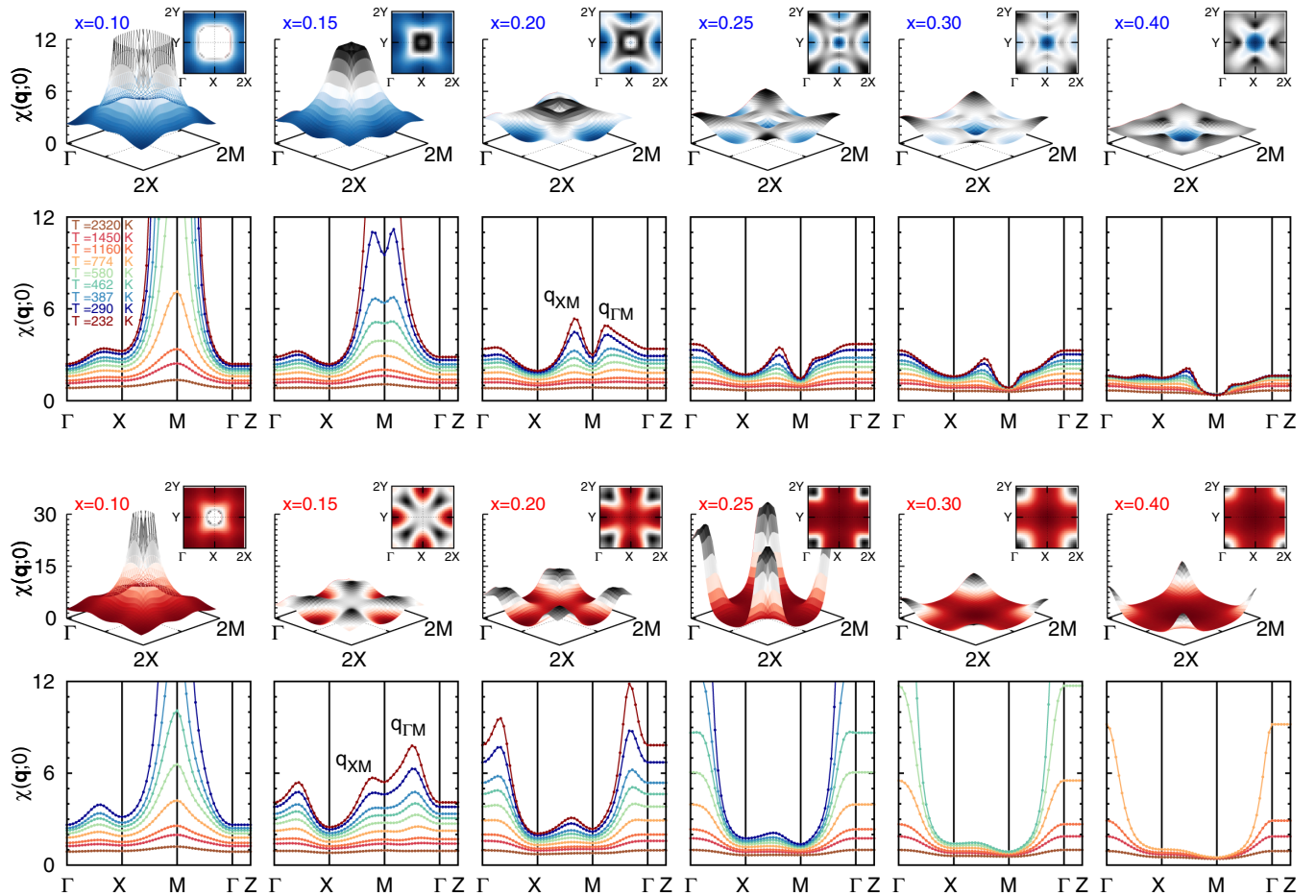


FIG. 9. Static lattice magnetic susceptibility for $t' = 0.2t$ (top panels) and $t' = 0.4t$ (bottom panels) for representative temperatures and along high-symmetry lines. From left to right x increases from 0.1 to 0.4. The three-dimensional plots and the contour plots on top of each figure show $\chi(\mathbf{q};0)$ for $T \sim 290$ K. For $t' = 0.4t$ and $x = 0.3$ or $x = 0.4$ the temperature chosen is right above the ferromagnetic transition. The special points are $\Gamma = (0, 0, 0)$, $M = (\pi, \pi, 0)$, $2M = (2\pi, 2\pi, 0)$, $X = (\pi, 0, 0)$, $2X = (2\pi, 0, 0)$, $Y = (0, \pi, 0)$, $2Y = (0, 2\pi, 0)$, $Z = (0, 0, \pi)$.

increases and then drops again (Fig. 7). For what concerns the incommensurate features, the extrapolated critical temperatures $T_C(\mathbf{q}_{\Gamma M})$ and $T_C(\mathbf{q}_{XM})$ strongly decrease; at $x = 0.2$ their value is already very small, making it less likely that static incommensurate spin structures can be realized for $x \geq 0.2$.

Two observations are in place. First, even in the $U = 0$ limit the susceptibility develops peaks at incommensurate vectors around M , as was often pointed out; for completeness, this is shown in Appendix A. Such peaks qualitatively evolve with x in a way similar to that in the finite- U case, although they do differ in many aspects, as may be seen comparing Fig. 9 to Fig. 18 in Appendix A. Second, the phenomenological nearly antiferromagnetic Fermi-liquid theory susceptibility [52], with a maximum at the antiferromagnetic vector (π, π) , approximates the results in Fig. 9 only up to max $x \sim 0.1$. Approaching optimal doping ($x \sim 0.15$) and going well beyond, the \mathbf{q} dependence qualitatively changes. Still, the change is only abrupt entering the overdoped regime ($x \sim 0.2$ and larger in the figure).

Let us now analyze the effect of increasing t' from $t' = 0.2t$ to $t' = 0.4t$. The main results as a function of x are shown in Fig. 9, bottom panels, and show that changes are large. For

$x \sim 0.10$ the static lattice susceptibility has a maximum at the M point, as for $t' = 0.2t$. The response at M is weaker, however, in line with the fact that we are still in the Curie-Weiss-like limit and frustration is increasing. For $x \sim 0.15$ again we find a change in behavior. At low temperature eventually incommensurate peaks develop around M ; this time, however, the area around M is strongly asymmetric for $x = 0.15$, as can be seen in the two-dimensional contours in the inset. Furthermore, the $\mathbf{q}_{\Gamma M}$ feature clearly dominates in the low temperature regime, but the associated mean-field critical temperature, again obtained as linear extrapolation, is as low as $\sim T_N/30$; again, $T_N = T_C(M)$ for $x = 0$. Increasing x , the asymmetry around the M point increases, \mathbf{q}_{XM} moves toward X and $\mathbf{q}_{\Gamma M}$ toward Γ , while at the same time the peak at $\mathbf{q}_{\Gamma M}$ grows taller; this eventually leads to dominant ferromagnetic instabilities for sufficiently large x . The increase in relevance of ferromagnetic correlations with x is also present for $U = 0$ (Appendix A), but the effect is less strong.

The trends obtained so far are qualitatively in line with the picture emerging from experimental facts. Summarizing, antiferromagnetic fluctuations at (π, π) dominate up to $x \sim 0.1$. They are then suppressed increasing x , eventually

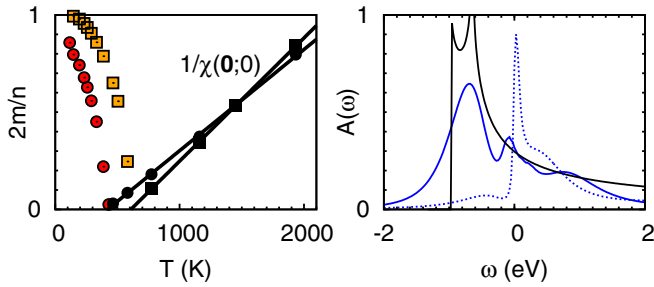


FIG. 10. Left: Normalized magnetization (symbols), defined as $2m/n = (n_{\uparrow} - n_{\downarrow})/(n_{\uparrow} + n_{\downarrow})$, and inverse static uniform susceptibility (symbols and lines) for $t' = 0.4t$ for $x \sim 0.30$ (circles) and $x \sim 0.40$ (squares). The fully polarized state with $m = 0.35$ is reached in the $T \rightarrow 0$ limit. The static susceptibility diverges $T \sim 430$ K for $x \sim 0.30$ and $T \sim 610$ K for $x \sim 0.40$. Right: Spin-resolved spectral function for $x = 0.3$ at 230 K. Black line: Noninteracting density of states. Full lighter line: Majority spin. Dashed line: Minority spin.

becoming unimportant in the overdoped regime. For $x \sim 0.15$ incommensurate features become dominant, to be quickly washed out further increasing x or suppressed by increasing t' . The static mean-field critical temperature for incommensurate instability at $\mathbf{q}_{\Gamma M}$ is about $T_N/10$ for $t' = 0.2t$ and $T_N/30$ for $t' = 0.4t$. Incommensurate stripes and spin waves are best known in the underdoped regime for the $\text{La}_{2-x}\text{B}_x\text{CuO}_4$ family, but have also been found in other cuprate families.

For $t' \sim 0.4t$ and $x \gtrsim 0.30$ we find a ferromagnetic phase (Fig. 10). A ferromagnetic phase was predicted by Kopp *et al.* [69] in overdoped cuprates via quantum critical scaling theory. Experimentally, in $\text{La}_{2-x}\text{Sr}_x\text{CuO}_4$ a potential low-temperature ferromagnetic phase [18] ($T < 2$ K) was reported at $x = 0.33$. Ferromagnetic fluctuations in the overdoped regime were recently found in $(\text{Bi,Pi})_2\text{Sr}_2\text{CuO}_{6+\delta}$ [79]. For the t - t' Hubbard model, $U \rightarrow \infty$ Nagaoka ferromagnetism was obtained in Ref. [77] for $t'/t = 0.1$, and it was shown to be suppressed for negative $t'/t = -0.1$. In this picture, the majority spin shows small mass renormalization, while the minority spin is highly correlated. Our results are Nagaoka-like, as the spectral functions in Fig. 10 show. Furthermore we find that the ferromagnetic state is favored by large x and t'/t , everything else staying the same. If t'/t is too small, the extrapolated Curie temperature becomes negative; i.e., even in mean-field theory no actual transition is expected. Ferromagnetism for finite U was also obtained very recently in Ref. [80] via a dynamical cluster approximation study; its origin was explained by mapping, via bonding and antibonding orbitals for 4-site plaquettes, the one-band Hubbard model into an equivalent two-orbital Hubbard model [81] with effective Coulomb parameters $\tilde{U} = \tilde{U}' = \tilde{J} = U/2$.

Figure 8 shows that for the static local susceptibility there are no qualitative changes in cDMFT calculations up to four-site clusters. Analyzing cluster effects in detail as a function of \mathbf{q} we find that nonlocal effects are more sizable approaching a phase transition and around the associated critical \mathbf{q} vector, reducing the transition temperatures [97]. Thus for $t' = 0.2t$ nonlocal correlations appear most important for $x \leq 0.1$ and close to the M point, where they decrease the value of the susceptibility; for $t' = 0.4t$ they are instead stronger for large x around the Γ point. At incommensurate vectors the effects

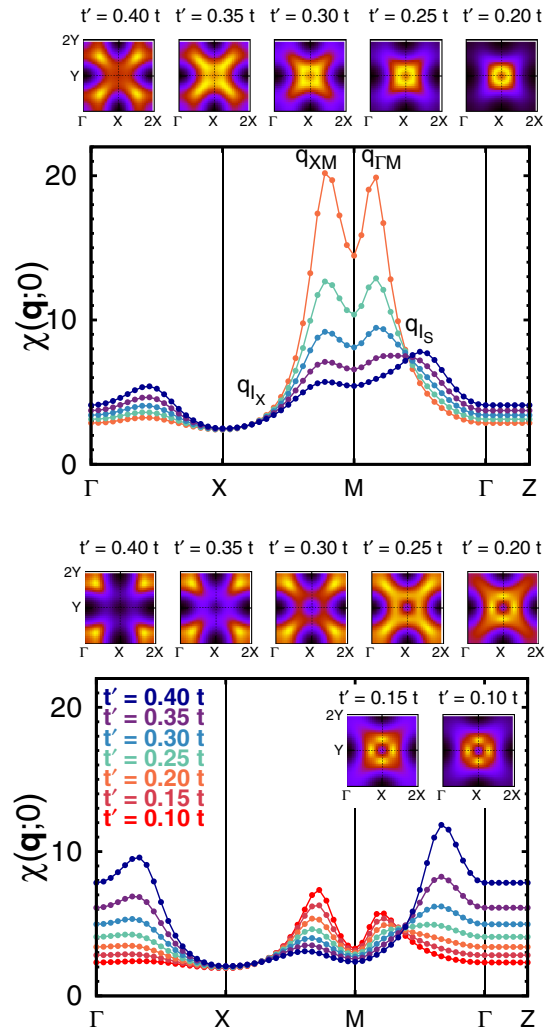


FIG. 11. Static lattice magnetic susceptibility for several t'/t . Calculations are performed for $U = 7$ eV and $T \sim 230$ K. Top: $x \sim 0.15$. Bottom: $x \sim 0.20$.

appear instead weaker. Overall, they do not affect in a qualitative way the trends so far.

E. Dependence of the static $x > 0$ susceptibility at finite \mathbf{q} on t'/t and U

In Fig. 11 we analyze the effects of systematically increasing t' for representative x values, below and above optimal doping. A similar behavior is found for all x values. The figure shows that the isosbestic point at \mathbf{q}_S , which we already discussed for $x = 0$, moves toward M with increasing x . The two isosbestic points which, for $x = 0$, were on the left and right of X (see Fig. 5) now collapse toward X , where a valley is formed (see label \mathbf{q}_X in the figure). The susceptibility changes strongly with increasing t' , but in an opposite way for \mathbf{q} vectors between \mathbf{q}_X and \mathbf{q}_S (it decreases) and for vectors outside this region (it increases). This is because of the sum rule [110] yielding the local susceptibility $\chi(0)$. In addition, while the incommensurate feature at \mathbf{q}_{XM} only slightly moves to the left when t' increases, progressively losing in strength, the one at $\mathbf{q}_{\Gamma M}$ moves rapidly away from M . Eventually it crosses \mathbf{q}_S

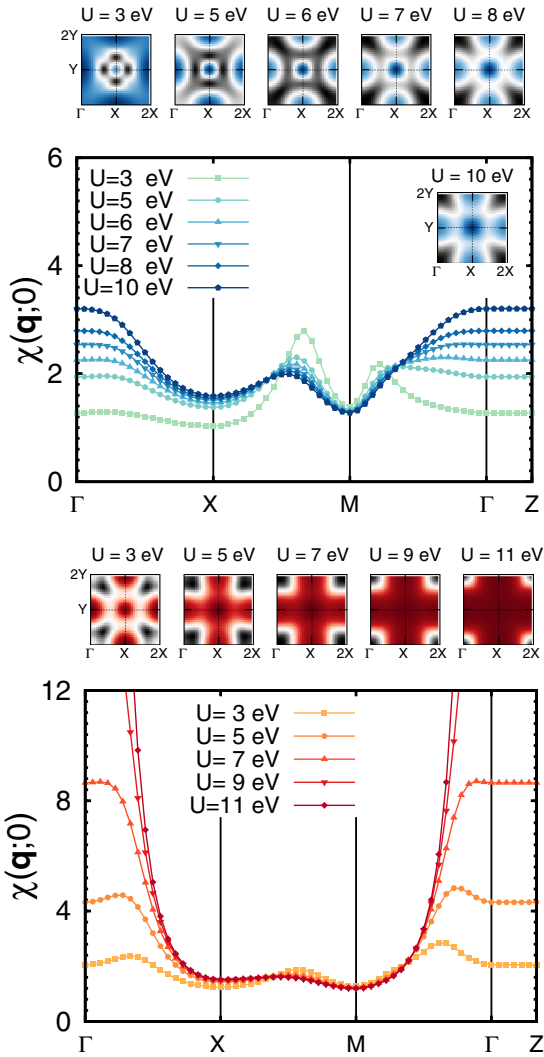


FIG. 12. DMFT static lattice magnetic susceptibility $\chi(\mathbf{q};0)$ for $x \sim 0.25$, $T \sim 460$ K, and different values of the Coulomb interaction. Top: $t' = 0.2t$. Bottom: $t' = 0.4t$.

and approaches Γ , this time gaining height, and dominating for large x values. This trend is perhaps more clear if we observe the evolution of the two-dimensional maps on the top of the panels. With increasing t'/t the four incommensurate maxima in $\chi(\mathbf{q};0)$ around M turn into a ring; eventually the ring changes into incommensurate maxima around the corners of the Brillouin zone. The switch occurs for larger x if t' is smaller, or, seen the other way around, for smaller t' if x is larger.

Last, we analyze the effects of varying the value of the screened Coulomb parameter U from 3 to 11 eV. The main conclusions are collected in Fig. 12 and in Fig. 13. In Fig. 12 we display results for $x \sim 0.25$, at which value two types of incommensurate features are present, and a possible instability toward ferromagnetism appears. Around M the response is slightly suppressed with increasing U , as one would expect when superexchange interactions between local moments dominate, but otherwise the behavior does not change qualitatively. Indeed, the larger differences are observed for $U = 3$ eV, which yields a metallic solution at half filling. Further

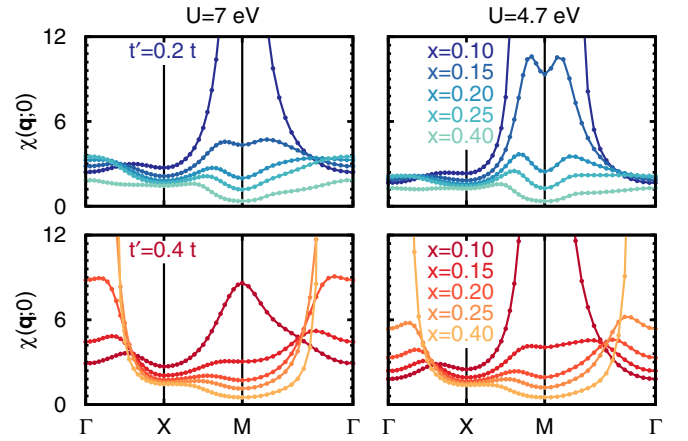


FIG. 13. DMFT static lattice magnetic susceptibility $\chi(\mathbf{q};0)$ at $T \sim 387$ K for several x and two representative U values. Top: $t' = 0.2t$. Bottom: $t' = 0.4t$.

reducing U to $U = 1$ eV yields a result which is closer to an enhanced noninteracting response, shown in Appendix A. The exact position of \mathbf{q}_{XM} is also moving with U , but the shift is small. The most remarkable effect of increasing U is that the response between $\mathbf{q}_{\Gamma S}$ and Γ increases very fast—much faster than expected from the reduction of the antiferromagnetic superexchange coupling, which can instead be seen for $x = 0$, Fig. 4. Furthermore $\mathbf{q}_{\Gamma M}$ rotates by 45 degrees and progressively moves toward Γ . This can be seen most clearly from the two-dimensional contour plots in the upper panels of the figure. Within the present description, the fact that ferromagnetism was found in $\text{La}_{2-x}\text{Sr}_x\text{CuO}_4$ for $x \sim 0.33$, although at very low temperatures [18], would suggest that the effective U cannot be too small. Increasing the value of t' to $t' = 0.4t$ the dominant features are always along ΓM and quickly move to Γ with increasing U , favoring a ferromagnetic instability at sufficiently low temperature.

Another important point is that even as a function of U we observe isosbestic points along the X - M - Γ direction. This may be seen clearly in the top panel of Fig. 12. They reflect the fact that the local susceptibility depends weakly on U till local moments persist—and this still happens well below U_c ; small deviations start to appear at $U \sim 3$ eV. The figure shows that, as a consequence, the effect of U changes across the isosbestic points. The \mathbf{q}_{XM} peak is more prominent the smaller U is, while the opposite happens around Γ . The figure thus confirms that the actual nature of the magnetic response is strongly \mathbf{q} dependent. While around M it is dominated by antiferromagnetic superexchange between local moments even for large x and relatively small U , around Γ it is metallic-like. The evolution with x is emphasized in Fig. 13, where we compare results for $U = 7$ eV and $U \sim U_c$. Here one may notice in addition that, as a function of x , the isosbestic points are only approximate and tend to disappear for large x .

F. NMR relaxation rate $1/T_1$

Next we calculate the NMR/NQR spin-lattice relaxation rate. It is defined via the relation [112]

$$\frac{1}{T_1 T} = \frac{\gamma^2}{2} \frac{1}{N_{\mathbf{q}}} \sum_{\mathbf{q}} F_{\perp}(\mathbf{q}) F_{\perp}(-\mathbf{q}) \lim_{\omega \rightarrow 0} \left(\frac{\chi''_{\perp}(\mathbf{q}; \omega)}{\omega} \right), \quad (18)$$

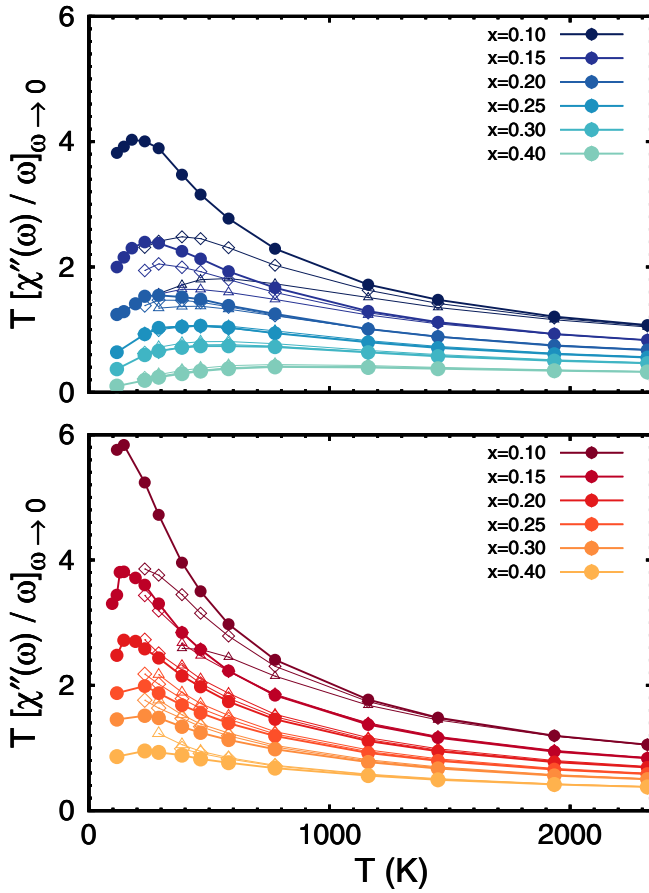


FIG. 14. Local ($\eta = 0$) contribution to the relaxation rate, calculated via DMFT (filled circles), 2S-cDMFT (rhombs), and 4S-cDMFT (triangles) for $t' = 0.2t$ (top), $t' = 0.4t$ (bottom), and several values of x .

where γ is the nuclear gyromagnetic ratio and $F_\alpha(\mathbf{q})$ the form factor for a magnetic field in direction α . At a ^{63}Cu site the form factor is given by $F_\alpha(\mathbf{q}) = A_\alpha + 4Bf_\alpha$; here $f_\alpha = (\cos q_x + \cos q_y)/2$, B is the (transferred) contact hyperfine field, and A_α the sum of the direct hyperfine interaction terms [51].

Experimentally, the relaxation rate anisotropy $R = T_{1c}/T_{1ab}$ was recently [44] found to be temperature independent, ranging from 1 to 3.4. This suggests that the temperature dependence of the relaxation rate should be captured already well by the local contribution. In DMFT and cDMFT calculations, this term can be obtained directly via the self-consistent quantum impurity problem, i.e., without solving the Bethe-Salpeter equation in addition. The result is displayed in Fig. 14 for two representative t'/t values and several x values. The figure shows that the local relaxation rate first increases with the temperature, reaches a maximum, and slowly decreases; for $x = 0.4$ for $t' = 0.2t$ the curve looks basically flat at high temperature; for $t' = 0$ qualitatively similar results were obtained in Ref. [113]. The maximum of the relaxation rate corresponds to $T \sim T_0(x)$ and it is thus more pronounced for small x and larger t' (lower panel, $x = 0.4$), i.e., when $T_0(x)$ is smaller, as we have previously discussed. The figure also shows, however, that for small x , the value of the

maximum and the temperature at which it is reached are not well captured by single-site DMFT. The maximum decreases with increasing cluster size; this happens because for small x the integrand is large at the M point, i.e., where nonlocal correlations are most important.

Figure 14 reasonably well reproduces some of the trends seen in experiments; for example it captures the decrease in relaxation rate in the normal state with increasing x observed in $\text{La}_{2-x}\text{Sr}_x\text{CuO}_4$ and $\text{YBa}_2\text{Cu}_3\text{O}_{6+y}$ [27,28,33,34,36]. There are remarkable differences, however. In $\text{La}_{2-x}\text{Sr}_x\text{CuO}_4$, NQR experiments found a basically x -independent plateau at about 700 K [42]. In $\text{YBa}_2\text{Cu}_4\text{O}_8$ a flattening of the relaxation rate occurs at about 400 K [45]. In Fig. 14, while all curves become close at very high temperatures, no such collapse to one universal value around 700 K for $t' = 0.2t$ is observed, or at lower temperature for larger t'/t , and a real flattening is only seen for $x = 0.4$ and $t' = 0.2$. This can be understood as follows. Our results show that the local relaxation rate and susceptibility satisfy approximately a local Korringa law

$$K = T_1^{(0)} T [\chi(0)]^2 \approx (0.43)^2, \quad (19)$$

where

$$\frac{1}{T_1^{(0)} T} = \lim_{\omega \rightarrow 0} \left(\frac{\chi''(\omega)}{\omega} \right). \quad (20)$$

Indeed, from Eq. (17), one may see that

$$\frac{(1-x)}{\chi(0)T_0(x)} \approx \frac{1 + T/T_0(x)}{(g\mu_B\mu_{\text{eff}})^2}. \quad (21)$$

This linear behavior is shown in the bottom panel of Fig. 15. We find that the relaxation rate, instead, scales approximately as follows:

$$\frac{(1-x)\sqrt{T_1^{(0)} T}}{T_0(x)} \approx \sqrt{K} \frac{1 + T/T_0(x)}{(g\mu_B\mu_{\text{eff}})^2}. \quad (22)$$

This is shown in the top panel of Fig. 15. Hence, the ratio of Eq. (22) and Eq. (21) yields, squared, the local Korringa ratio. For $T \gg T_0(x)$ the tails of $1/T_1$ depend on x via the effective moment, which decreases with x increasing. The flattening in Fig. 14 for $t' = 0.4t$ and $x = 0.2$ is thus an effect of $T_0(x)$ being large. Nonlocal effects, on the other hand, increase $T_0(x)$, as may be seen in Fig. 14. This makes the curves look more flat for a given x ; it does not, however, cancel out the x dependence of the tails. Furthermore, experimentally [34,36,44], the ^{63}Cu relaxation rates are visibly larger in $\text{La}_{2-x}\text{Sr}_x\text{CuO}_4$ than in $\text{Tl}_2\text{Ba}_2\text{CuO}_6$ or $\text{YBa}_2\text{Cu}_3\text{O}_{6+y}$. A trend in this direction does not emerge in Fig. 14 simply increasing t'/t for a given x , however. In the picture so far, it can only be ascribed to the differences in hole doping, with $\text{Tl}_2\text{Ba}_2\text{CuO}_6$ being in the overdoped regime.

In Fig. 16 we summarize the effects of the form factor $F_\perp(\mathbf{q})$. To this end we first split the ^{63}Cu relaxation rate into three components, which we label as $1/T_1^{(\eta)}$, with $\eta = 0, 1, 2$. They are obtained as

$$\frac{1}{T_1^{(\eta)} T} = \frac{1}{N_{\mathbf{q}}} \sum_{\mathbf{q}} w_\eta(\mathbf{q}) \lim_{\omega \rightarrow 0} \left(\frac{\chi''(\mathbf{q}; \omega)}{\omega} \right), \quad (23)$$

with $w_\eta(\mathbf{q}) = (-2f_\alpha)^\eta$. The $\eta = 0$ component gives the local contribution to the relaxation rate shown in Fig. 14. The left

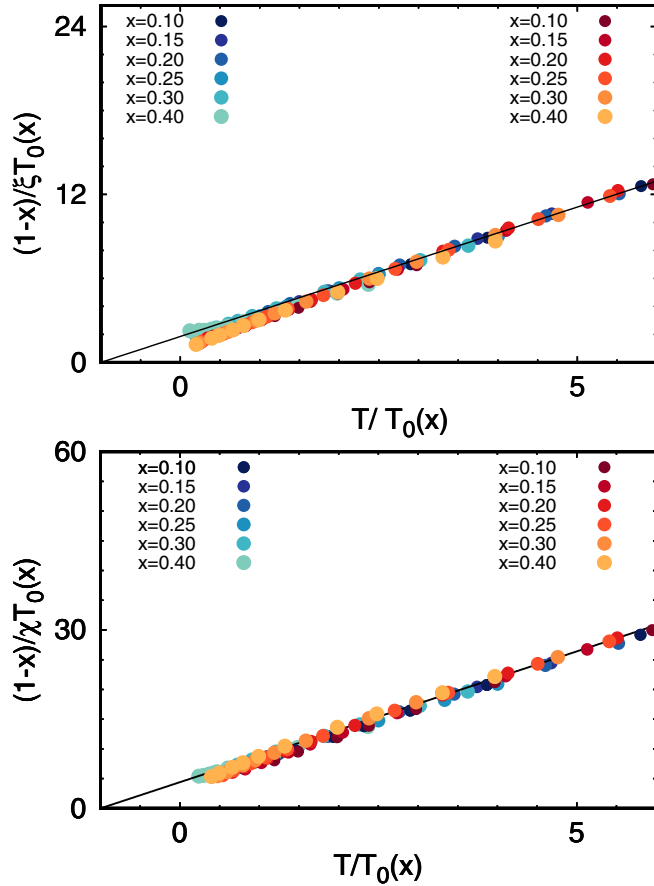


FIG. 15. Top: Normalized inverse square root of the spin-lattice relaxation rate. Here $\xi = [1/T_1^{(0)}T]^{1/2}$. Bottom: Normalized inverse Knight shift. The notation is the same as in Fig. 14.

panels of Fig. 16 show that the $\eta = 0$ and $\eta = 2$ components of the relaxation rate yield a similar contribution, since the response function is weak at the X point; the $\eta = 1$ term remains small in comparison, and tends to become negative increasing U and t' , decreasing the anisotropy and $1/T_1^{ab}$. Including the $\eta = 1, 2$ terms has stronger effects, however, through the hyperfine fields. While A_c and A_{ab} are typically considered weakly material dependent, the transferred field B (extracted by fitting the experimental Knight shifts) was found to be strongly affected by the environment and doping [31,34,56]. Theoretically, this is supported by electronic-structure calculations showing that also B depends on the energy $\tilde{\epsilon}$, of the axial orbital [53]; for single-layered materials, in first approximation, B thus increases for the same reasons for which t' increases [62]. In phenomenological theories, to explain the fact that in $\text{YBa}_2\text{Cu}_3\text{O}_7$ and $\text{La}_{2-x}\text{Sr}_x\text{CuO}_4$ the K_c ^{63}Cu Knight shift is temperature independent below T_c , an accidental cancellation $4B + A_c \sim 0$ is typically assumed. Based on these premises, values of B two or even three times larger were estimated for $\text{Tl}_2\text{Ba}_2\text{CuO}_{6+y}$ [31,34], with the maximum value for the sample with no superconducting phase. Figure 16 shows (top right panel) that for fixed B , the in-plane relaxation rate is larger for smaller t'/t , while the opposite can happen if the field is along c (bottom right panel). Increasing B of a factor two, everything else staying the same, can

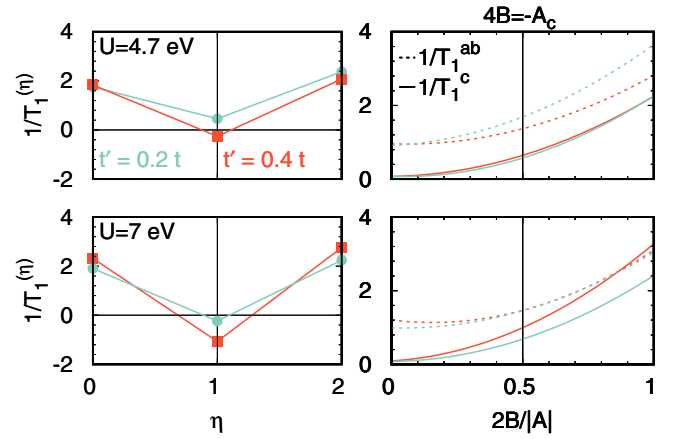


FIG. 16. Left: Contributions $1/T_1^{(n)}$ to the relaxation rate for $x = 0.15$ (close to optimal doping), $t' = 0.2t$ and $t' = 0.4t$ at 580 K, in the temperature regime $T \sim aT_0(x)$, with $a \in (1, 2)$. Right: $1/T_1^c$ and $1/T_1^a$ as a function of $y = 2B/|A_c|$. They are defined in units of A_c as $1/T_1^c = r_A^2/T_1^{(0)} + y^2/T_1^{(2)} - 2r_{AY}/T_1^{(1)}$ and $1/T_1^{ab} = \frac{1}{2}(1 + r_A^2)/T_1^{(0)} + y^2/T_1^{(2)} + y(1 - r_A)/T_1^{(1)}$, where $r_A = A_{ab}/|A_c|$ and $A_c \sim -5A_{ab}$. The vertical line corresponds to $4B = -A_c$.

increase sizably the relaxation rate; this is because the only term that can reduce it, the linear $\eta = 1$ contribution, is small in comparison to the quadratic $\eta = 2$ term. Furthermore, for sufficiently large B and U one could, in principle, even reverse the sign of the anisotropy. On the other hand, we find that increasing x , everything else staying the same, reduces $1/T_1^{(0)}$ and $1/T_1^{(2)}$, reducing the average relaxation rate, and makes $1/T_1^{(1)}$ more negative, reducing the anisotropy. In conclusion, in the picture emerging from these results, if we assume that the experimental B values are approximately correct, a smaller relaxation rate in $\text{Tl}_2\text{Ba}_2\text{CuO}_{6+y}$ should be mostly ascribed to the fact that this system is well inside the overdoped regime.

More complicated is to conciliate the theoretical results with the x -independent plateau at 700 K in $\text{La}_{2-x}\text{Sr}_x\text{CuO}_4$. In this system, B is often considered almost doping independent, in order to explain the fact that the perpendicular Knight shift does not drop below T_c , and does not change much in absolute value. A certain amount of x dependence is still compatible with NMR experiments, however [56]. An increase of B could in principle compensate the decrease associated with the reduction in effective local moment. It has to be noticed, however, that a universal plateau would require a (second) accidental cancellation and a sufficiently large $T_0(x)$, a delicate equilibrium of factors. If this is the case, it should be possible to observe that the universality is broken by measuring spin-lattice relaxation rates with magnetic field in different directions.

G. Bosonic spin excitations

Bosonic spin excitations in cuprates have been intensively studied, and have evidenced features common to several cuprates [2,3]. Among those are resonance peaks [7,14,15] around M in the range 50–70 meV as well as incommensurate low-energy excitations [6,8,10]. With time, evidence of a seemingly “universal” X-shaped behavior of spin excitations

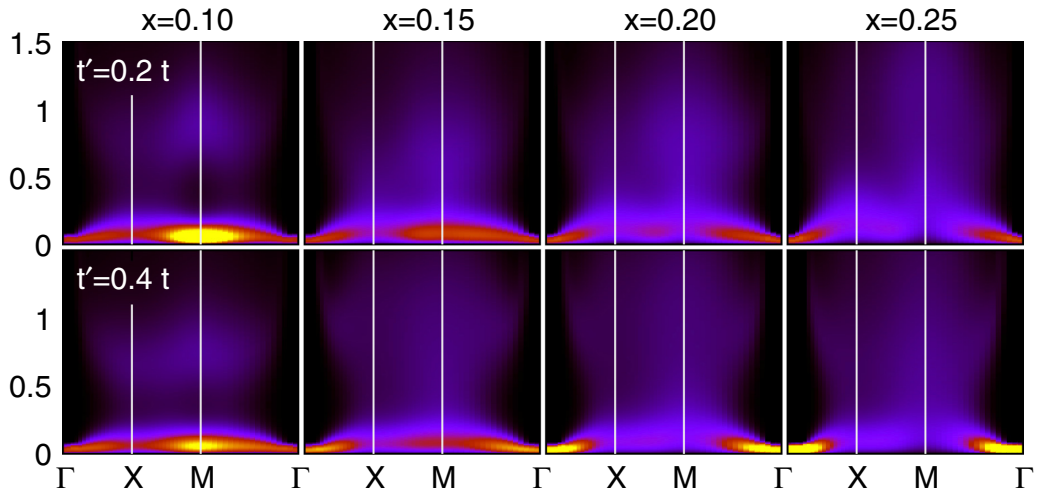


FIG. 17. Dynamical susceptibility (intensity maps) for $t' = 0.2t$ (top) and $t' = 0.4t$ (bottom) and increasing x in the paramagnetic phase, $U = 7$ eV. The special points are $\Gamma = (0, 0)$, $X = (\pi, 0)$, and $M = (\pi, \pi)$. The spectra do not change much, further increasing x to 0.4.

in underdoped cuprates accumulated, with perhaps the exception of $\text{HgBa}_2\text{CuO}_{4+\delta}$ [46].

Theoretically, the x dependence of spin excitations has been studied with various techniques and models [22,65,114,115]. Recently, it has been shown via the dual boson approach [68] that in the underdoped region the dominant spin excitations remain close to the M point. Our results are in line with this conclusion, as one can see in Fig. 17, left panels. For small x the low-energy spectra have a form similar to the one we obtained for $x = 0$ (see Fig. 6) with a maximum at M which persists till optimal doping. As in the $x = 0$ case, we find that the spectra are very similar decreasing U to U_c , leaving a slightly larger dispersion aside. Figure 17 also shows that, at sufficiently low frequency, the calculated modes reflect the behavior of the static susceptibility and the \mathbf{q} -resolved relaxation rate. Finally, the spectrum is qualitatively very similar for $t' = 0.2t$ and $t' = 0.4t$, although the intensity at the M point decreases in absolute value increasing t' . The energy of the maximum at M is compatible with the resonance modes.

Increasing x beyond the underdoped regime the situation changes. Although a shadow of the original mode stays, already at optimal doping the maximum weight starts to move away from the M point. One can then identify incommensurate features at \mathbf{q}_{XM} and $\mathbf{q}_{\Gamma M}$, as for the static susceptibility. For $x = 0.25$ the weight is already mostly at Γ . Qualitatively the trend remains the same for $t' = 0.2t$ and $t' = 0.4t$, but when t' is larger, the figure shows that the intensity moves faster toward the Γ point. This indicates that the bosonic spin excitations, within the present modeling, are not, at the core, really universal, although the shade of the small x spectra does persist even for large x ; below $x = 0.15$ the spectra look very similar, however.

IV. CONCLUSIONS

We have studied the static and dynamical magnetic properties of the t - t' Hubbard model in a parameter regime relevant for high-temperature superconducting cuprates. When possible, we complement numerical results with approximate analytic expressions. Our calculations confirm previous

conclusions [61,65–68,70–77] showing that the electronic properties are very sensitive to the value of t'/t . In addition, we find a sharp change in behavior entering the overdoped regime.

At half filling ($x = 0$), the calculated spin-wave spectra are close to those obtained from standard spin-wave theory, both in the paramagnetic and magnetic phase. This remains true even for U approaching the insulator-to-metal transition; in this regime, the spin-wave spectrum is enhanced, however, due to the smaller charge fluctuation energy. The trends with t'/t are approximately in line with experimental observations so far.

For $x \neq 0$, the nonmonotonic evolution of the uniform susceptibility, reported for thermodynamics experiments in $\text{La}_{2-x}\text{Sr}_x\text{CuO}_4$, is fully captured by the model. The turning point tends to move to larger x by increasing t' . The case of overdoped $\text{Tl}_2\text{Ba}_2\text{CuO}_{6+y}$ appears a further confirmation of the trend. Also captured is the tendency toward the formation of incommensurate structures for small x and in systems characterized by a relatively small t' . For very large x and t' ferromagnetic instabilities are favored instead.

The results obtained show that the nature of the magnetic response is strongly \mathbf{q} dependent. Isosbestic points mark regions of the Brillouin zone exhibiting different scaling with the parameters U , t'/t , T . Thus, scaling laws obtained, e.g., from the uniform susceptibility and Knight shifts, should not be automatically extended to experiments probing other parts of the Brillouin zone, or to local responses. Ferromagnetic instabilities are suppressed for sufficiently small U .

The material dependence of the experimental relaxation rates appears more problematic to describe. While qualitatively the temperature and x dependence are in line with experiments, some remarkable observations are not quantitatively reproduced. In particular, the universal (x -independent) high-temperature plateau in $\text{La}_{2-x}\text{Sr}_x\text{CuO}_4$ would require accidental cancellations. Instead, the fact that the relaxation rate is smaller in $\text{Tl}_2\text{Ba}_2\text{CuO}_{6+y}$ than $\text{La}_{2-x}\text{Sr}_x\text{CuO}_4$ could be ascribed to overdoping. The difficulties in describing trends in spin-lattice relaxation rates can be due to the intrinsic complexity of NMR/NQR experiments, e.g., the fact that some of

the current assumptions on hyperfine fields are incorrect, or that further channels have to be explicitly taken into account [43,44].

Finally, bosonic excitations appear robust under changes in t' up to close to optimal doping. For larger x the intensity shifts toward Γ going through incommensurate features, although the shadow of the antiferromagnetic mode remains for much larger x . These results complement those obtained recently with different techniques; e.g., for $t' = 0.3t$ an intensity transfer toward Γ was found in Ref. [22] using the determinant quantum Monte Carlo approach; for small x and t' a stable structure of paramagnons at M was obtained in Ref. [68] via the dual-boson method.

In conclusion, together with the successes, we discussed some limitations of the single-band picture, which indicate that experimental observations, in particular the description of NMR/NQR relaxation rates, require a more realistic modeling [62,63] to fully account for the differences between families of superconducting cuprates.

ACKNOWLEDGMENTS

The authors gratefully acknowledge the Gauss Centre for Supercomputing e.V. [116] for funding this project by providing computing time on the GCS Supercomputer JUWELS at Jülich Supercomputing Centre (JSC). We acknowledge financial support from the Deutsche Forschungsgemeinschaft through RTG 1995 and the former research unit FOR 1346.

APPENDIX A: LATTICE MAGNETIC SUSCEPTIBILITY CLOSE TO HALF FILLING, $T > T_N$

In the small- t/U and small- x limit, neglecting the metallic contribution (two-pole approximation), an approximate form of the local self-energy is [117,118]

$$\Sigma^\sigma(i\nu_n) \sim Un_{-\sigma} + \frac{n_{-\sigma}(1-n_{-\sigma})U^2r_0^2}{i\nu_n + \mu - \mathcal{B}_\sigma - U(1-n_{-\sigma})}, \quad (\text{A1})$$

where $n_\sigma = n/2 = (1-x)/2$ is the number of particles with spin σ , μ the chemical potential, and $\mathcal{B}_\sigma = \sum_{ij} t_{ij} \langle c_{i\sigma}^\dagger c_{j\sigma} \rangle (2n_{i,-\sigma} - 1)$ is a shift which increases with x ; in the paramagnetic phase all quantities are spin independent. The factor r_0 is obtained fitting the numerical self-energy; for $r_0 = 1$ and $n = 1$, Eq. (A1) equals the atomic self-energy at half filling. Within this approximation, setting $\mu' = \mu - \mathcal{B} - nU/2$ and $n = 1 - x$, the Green's function takes the two-pole form

$$G_\sigma(\mathbf{k}; i\nu_n) = \frac{\frac{E_{\mathbf{k}}^+ - Ux + \mu'}{i\nu_n - E_{\mathbf{k}}^+} - \frac{E_{\mathbf{k}}^- - Ux + \mu'}{i\nu_n - E_{\mathbf{k}}^-}}{E_{\mathbf{k}}^+ - E_{\mathbf{k}}^-}}, \quad (\text{A2})$$

where

$$E_{\mathbf{k}}^\pm = Ux - \mu' + \frac{1}{2}(\varepsilon_{\mathbf{k}} - xU - \mathcal{B} \pm \Delta E_{\mathbf{k}}), \quad (\text{A3})$$

$$\Delta E_{\mathbf{k}} = \sqrt{(\varepsilon_{\mathbf{k}} - xU - \mathcal{B})^2 + (1-x^2)U^2r_0^2}, \quad (\text{A4})$$

and $\varepsilon_{\mathbf{k}}$ is the band dispersion. After performing the Matsubara sum, in the limit of large βU we obtain

$$\chi_0(\mathbf{q}; 0) \approx \frac{(g\mu_B\mu_{\text{eff}})^2}{r_0U} \left\{ c_1(x) - \frac{c_2(x)}{2U} \left[J_{r_0}(\mathbf{0}) + \frac{1}{2}J_{r_0}(\mathbf{q}) \right] \right\},$$

where $\mu_{\text{eff}} \sim \sqrt{S(S+1)/3}$ and

$$c_1(x) = \frac{1-x^2}{d^{3/2}}, \quad (\text{A5})$$

$$c_2(x) = \frac{1-x^2}{d^{5/2}} \left(1 - \frac{5b^2}{d} \right), \quad (\text{A6})$$

with $d = 1 - x^2 + b^2$ and $b = x/r_0 + \mathcal{B}/Ur_0$. The effective exchange coupling is defined as $J_{r_0}(\mathbf{q}) = J_{SE}(\mathbf{q})/2r_0^2$. In the small- x limit the coefficients become $c_1(x) = 1 + o_1(x^2)$ and $c_2(x) = 1 + o_2(x^2)$. At first order in x , the associated local susceptibility is thus given by

$$\chi_0(0) \approx \frac{(g\mu_B\mu_{\text{eff}})^2}{r_0U} \left[1 - \frac{1}{2U}J_{r_0}(\mathbf{0}) \right]. \quad (\text{A7})$$

Next we approximate the total local susceptibility with the atomic susceptibility in the large $\beta U \gg 1$ limit, assuming negligible double occupations. Thus

$$\chi(0) \sim \frac{(g\mu_B\mu_{\text{eff}})^2}{k_B T} (1-x). \quad (\text{A8})$$

Consequently, the vertex function is given by

$$\Gamma(0) = [\chi_0(0)]^{-1} - [\chi(0)]^{-1} \approx \frac{1}{(g\mu_B\mu_{\text{eff}})^2} \left\{ r_0U \left(1 + \frac{J_{r_0}(\mathbf{0})}{2U} \right) - \frac{k_B T}{1-x} \right\}. \quad (\text{A9})$$

The lattice magnetic susceptibility takes then the form

$$\chi(\mathbf{q}; 0) \approx \frac{(g\mu_B)^2 \mu_{\text{eff}}^2 (1-x)}{k_B T + \mu_{\text{eff}}^2 (1-x) r_0 J_{r_0}(\mathbf{q})}. \quad (\text{A10})$$

This formula is a generalization of the one derived in Ref. [100] for the case of half filling. For comparison, the noninteracting susceptibility is shown in Fig. 18 for increasing x .

APPENDIX B: STATIC AND DYNAMICAL LATTICE SUSCEPTIBILITY AT HALF FILLING FOR $T \ll T_N$

In the magnetic phase the local self-energy matrix can be approximated by its Hartree-Fock contribution. Thus $\Sigma_\sigma^i(i\nu_n) \approx -\mu + s_i \sigma m U$, where $m \sim 1/2$ is the magnetization, i is the site, and $s_i = \pm 1$, alternating for neighboring Cu sites; the number of sites in the unit cell is $n_i = 2$. As a consequence, for a given spin quantum number σ , we can write the associated $n_i \times n_i$ Green's function matrix as follows:

$$G_\sigma(\mathbf{k}; i\nu_n) = \frac{1}{D_{\mathbf{k}}(i\nu_n)} \begin{pmatrix} i\nu_n - \gamma_{\mathbf{k}} - \sigma m U & \alpha_{\mathbf{k}} e^{-ik_x a} \\ \alpha_{\mathbf{k}} e^{ik_x a} & i\nu_n - \gamma_{\mathbf{k}} + \sigma m U \end{pmatrix}, \quad (\text{B1})$$

where

$$D_{\mathbf{k}}(i\nu_n) = (i\nu_n - \gamma_{\mathbf{k}})^2 - (\alpha_{\mathbf{k}}^2 + (mU)^2). \quad (\text{B2})$$

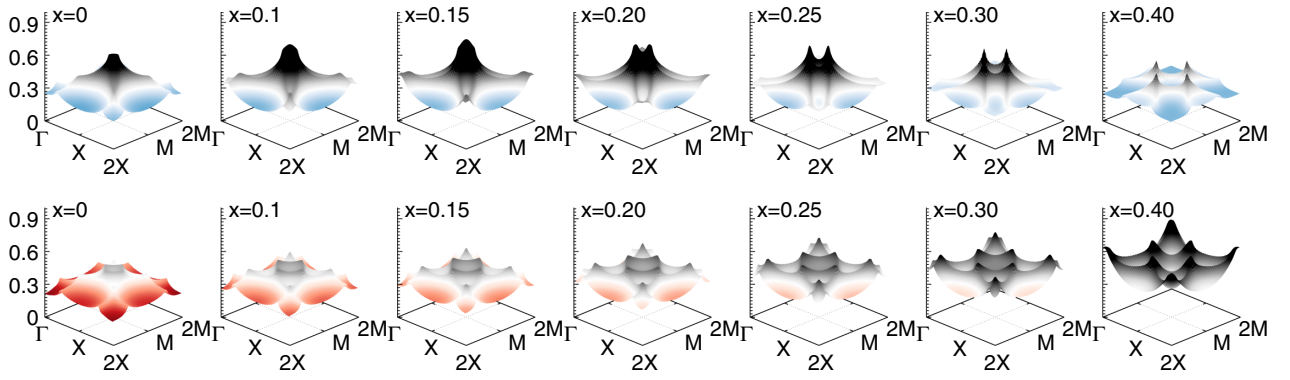


FIG. 18. The noninteracting magnetic response function for $t' = 0.2t$ (top panels) and $t' = 0.4t$ (bottom panels) in the $T \rightarrow 0$ limit.

Here $\alpha_{\mathbf{k}} = -2t(\cos k_x + \cos k_y)$ and $\gamma_{\mathbf{k}} = 4t' \cos k_x \cos k_y$, so that $\varepsilon_{\mathbf{k}} = \alpha_{\mathbf{k}} + \gamma_{\mathbf{k}}$. Let us introduce the energies

$$E_{\mathbf{k}}^{\pm} = \gamma_{\mathbf{k}} \pm \sqrt{\alpha_{\mathbf{k}}^2 + (mU)^2} = \gamma_{\mathbf{k}} \pm \Delta\alpha_{\mathbf{k}}. \quad (\text{B3})$$

The elements of the Green's function matrix can then be expressed as

$$G_{\sigma}^{ii'}(\mathbf{k}; i\nu_n) = \sum_{p=\pm} \frac{w_{\sigma\mathbf{k}p}^{ii'}}{i\nu_n - E_{\mathbf{k}}^p}. \quad (\text{B4})$$

The weights are given by

$$w_{\sigma\mathbf{k}p}^{11} = \frac{1}{2} \left(1 - p \frac{\sigma mU}{\sqrt{\alpha_{\mathbf{k}}^2 + (mU)^2}} \right) = w_{-\sigma\mathbf{k}p}^{22} \quad (\text{B5})$$

and

$$w_{\sigma\mathbf{k}p}^{12} = \frac{p}{2} \frac{\alpha_{\mathbf{k}}}{\sqrt{\alpha_{\mathbf{k}}^2 + (mU)^2}} e^{-ik_x a} = [w_{\sigma\mathbf{k}p}^{21}]^*. \quad (\text{B6})$$

We can now calculate the elements of the lattice susceptibility tensor

$$\chi_{\sigma\sigma'\sigma''\sigma}^{0:ii'}(\mathbf{q}; i\omega_m) = \frac{-1}{\beta N_{\mathbf{k}}} \sum_{\mathbf{k}n} G_{ii'}^{\sigma}(\mathbf{k}; i\nu_n) G_{\sigma'\sigma''}^{\sigma'}(\mathbf{k} + \mathbf{q}; i\nu_n + i\omega_m). \quad (\text{B7})$$

Summing over the fermionic Matsubara frequency this expression simplifies to the sum given below:

$$\chi_{\sigma\sigma'\sigma''\sigma}^{0:ii'}(\mathbf{q}; i\omega_m) \approx -\frac{1}{N_{\mathbf{k}}} \sum_{\mathbf{k}} \sum_{pp'} w_{\sigma\mathbf{k}p}^{ii'} w_{\sigma'\mathbf{k}+\mathbf{q}p'}^{i'i} I_{\mathbf{k},\mathbf{q}}^{pp'}(i\omega_m), \quad (\text{B8})$$

where

$$I_{\mathbf{k},\mathbf{q}}^{pp'}(i\omega_m) = \beta n_F(E_{\mathbf{k}}^p) [n_F(E_{\mathbf{k}}^p) - 1] \delta_{\omega_m, 0} \delta(E_{\mathbf{k}}^p, E_{\mathbf{k}+\mathbf{q}}^p) \quad (\text{B9})$$

$$+ \frac{n_F(E_{\mathbf{k}}^p) - n_F(E_{\mathbf{k}+\mathbf{q}}^p)}{i\omega_m + E_{\mathbf{k}}^p - E_{\mathbf{k}+\mathbf{q}}^p} [1 - \delta_{\omega_m, 0} \delta(E_{\mathbf{k}}^p, E_{\mathbf{k}+\mathbf{q}}^p)]. \quad (\text{B10})$$

Here $n_F(\varepsilon)$ is the Fermi distribution function. This formula shows that the elements of the static susceptibility tensor go to zero in the zero-temperature limit. Assuming that the quan-

tization axis \hat{z} is also the magnetization axis, the longitudinal and transfer susceptibilities are defined as follows:

$$\chi_0^{\parallel}(\mathbf{q}; i\omega_m) = \frac{(g\mu_B)^2}{4} \sum_{\sigma} \frac{1}{2} \sum_{ii'} \chi_{\sigma\sigma\sigma\sigma}^{0:ii'}(\mathbf{q}; i\omega_m) e^{i\phi_{\mathbf{q}}^{ii'}}, \quad (\text{B11})$$

$$\chi_0^{\perp}(\mathbf{q}; i\omega_m) = \frac{(g\mu_B)^2}{4} \sum_{\sigma} \frac{1}{2} \sum_{ii'} \chi_{-\sigma\sigma\sigma-\sigma}^{0:ii'}(\mathbf{q}; i\omega_m) e^{i\phi_{\mathbf{q}}^{ii'}}, \quad (\text{B12})$$

where $\phi_{\mathbf{q}}^{ii'} = (1 - \delta_{ii'})(-1)^i q_x a$. Summing over the sites and spin quantum numbers we thus obtain

$$\chi_0^{\alpha}(\mathbf{q}; i\omega_m) \sim -\frac{(g\mu_B)^2}{4} \frac{1}{N_{\mathbf{k}}} \sum_{\mathbf{k}} \sum_{pp'=\pm} v_{\mathbf{k},\mathbf{q}}^{\alpha,pp'} I_{\mathbf{k},\mathbf{q}}^{pp'}(i\omega_m) e^{i\phi_{\mathbf{q}}^{ii'}}, \quad (\text{B13})$$

where $\alpha = \parallel, \perp$. The weights are defined as

$$v_{\mathbf{k},\mathbf{q}}^{\parallel,pp'} = \frac{1}{2} \left(1 + pp' \frac{\alpha_{\mathbf{k}} \alpha_{\mathbf{k}+\mathbf{q}} + (mU)^2}{\Delta\alpha_{\mathbf{k}} \Delta\alpha_{\mathbf{k}+\mathbf{q}}} \right), \quad (\text{B14})$$

$$v_{\mathbf{k},\mathbf{q}}^{\perp,pp'} = \frac{1}{2} \left(1 + pp' \frac{\alpha_{\mathbf{k}} \alpha_{\mathbf{k}+\mathbf{q}} - (mU)^2}{\Delta\alpha_{\mathbf{k}} \Delta\alpha_{\mathbf{k}+\mathbf{q}}} \right). \quad (\text{B15})$$

In the low-temperature limit only the $I_{\mathbf{k},\mathbf{q}}^{pp'}$ terms with $p' = -p$ contribute. This has consequences for the behavior of the dynamical susceptibility. Let us consider first the case of the longitudinal response function. The weight $v_{\mathbf{k},\mathbf{q}}^{\parallel,pp}$ is finite for every \mathbf{q} vector; it takes its maximum value at the Γ point ($v_{\mathbf{k},\mathbf{0}}^{\parallel,pp} = 1$). The weight $v_{\mathbf{k},\mathbf{q}}^{\parallel,p-p}$, however, is of order $4t^2/U^2$ and goes to zero at the Γ point. The situation is opposite for the transverse susceptibility. The weight $v_{\mathbf{k},\mathbf{q}}^{\perp,p-p}$ is maximum ($v_{\mathbf{k},\mathbf{M}}^{\perp,p-p} = 1$) at the M point and, furthermore, it remains close to one for all values of \mathbf{q} .

In the low-temperature limit (in which $m \sim 1/2$), setting $t' = 0$ for simplicity, at finite frequency we obtain in the small- t/U limit the approximate expression

$$\chi_{\sigma-\sigma-\sigma\sigma}^{0:ii'}(\mathbf{q}; i\omega_m) \approx \left[-\frac{a_{\sigma}^{ii'}(\mathbf{q})}{i\omega_m - U} + \frac{a_{-\sigma}^{i'i}(\mathbf{q})}{i\omega_m + U} \right] e^{-i\phi_{\mathbf{q}}^{ii'}}, \quad (\text{B16})$$

where

$$a_{\sigma}^{11}(\mathbf{q}) = a_{-\sigma}^{22}(\mathbf{q}) \approx \frac{1}{4} \left[1 - \sigma \left(1 - \frac{2J_1}{U} \right) \right]^2, \quad (\text{B17})$$

$$a_{\sigma}^{12}(\mathbf{q}) = a_{-\sigma}^{21}(\mathbf{q}) \approx -\frac{J_1}{U} f_{\mathbf{q}}, \quad (\text{B18})$$

and $f_{\mathbf{q}} = (\cos q_x + \cos q_y)/2$. By inverting the susceptibility matrix with the elements defined above we thus obtain at linear order in J_1 the matrix with elements

$$\left[\frac{1}{\chi^0(\mathbf{q}; i\omega_m)} - \frac{1}{\chi^0(i\omega_m)} \right]_{\sigma-\sigma-\sigma\sigma}^{ii'} \approx 2J_1 f_{\mathbf{q}} (1 - \delta_{ii'}) e^{-i\phi_{\mathbf{q}}^{ii'}}. \quad (\text{B19})$$

By adding to this the inverse of the local susceptibility matrix and multiplying for the prefactors, we finally have

$$\chi^{\perp}(\mathbf{q}; i\omega_m) \sim (g\mu_B)^2 \frac{J_1(1 - f_{\mathbf{q}})}{\omega_m^2 + 4J_1^2(1 - f_{\mathbf{q}}^2)}, \quad (\text{B20})$$

which is the expected behavior for a Heisenberg antiferromagnet.

-
- [1] J. G. Bednorz and K. A. Müller, *Z. Phys. B* **64**, 189 (1986).
- [2] J. R. Schrieffer and J. S. Brooks, editors, *Handbook of High-Temperature Superconductivity. Theory and Experiments* (Springer Science + Business Media, New York, 2007), and references therein.
- [3] N. Plakida, *High-Temperature Cuprate Superconductors*, Springer Series in Solid-State Sciences (Springer, New York, 2010), and references therein.
- [4] G. Shirane, Y. Endoh, R. J. Birgeneau, M. A. Kastner, Y. Hidaka, M. Oda, M. Suzuki, and T. Murakami, *Phys. Rev. Lett.* **59**, 1613 (1987).
- [5] R. Coldea, S. M. Hayden, G. Aeppli, T. G. Perring, C. D. Frost, T. E. Mason, S.-W. Cheong, and Z. Fisk, *Phys. Rev. Lett.* **86**, 5377 (2001).
- [6] K. Yamada, C. H. Lee, K. Kurahashi, J. Wada, S. Wakimoto, S. Ueki, H. Kimura, Y. Endoh, S. Hosoya, G. Shirane, R. J. Birgeneau, M. Greven, M. A. Kastner, and Y. J. Kim, *Phys. Rev. B* **57**, 6165 (1998).
- [7] H. A. Mook, M. Yethiraj, G. Aeppli, T. E. Mason, and T. Armstrong, *Phys. Rev. Lett.* **70**, 3490 (1993).
- [8] S.-W. Cheong, G. Aeppli, T. E. Mason, H. Mook, S. M. Hayden, P. C. Canfield, Z. Fisk, K. N. Clausen, and J. L. Martinez, *Phys. Rev. Lett.* **67**, 1791 (1991).
- [9] P. Dai, H. A. Mook, S. M. Hayden, G. Aeppli, T. G. Perring, H. A. Mook, and F. Dogan, *Science* **284**, 1344 (1999).
- [10] H. A. Mook, P. Dai, S. M. Hayden, G. Aeppli, T. G. Perring, and F. Dogan, *Nature (London)* **395**, 580 (1998).
- [11] P. Bourges, H. Casalta, A. S. Ivanov, and D. Petitgrand, *Phys. Rev. Lett.* **79**, 4906 (1997).
- [12] S. M. Hayden, G. Aeppli, T. G. Perring, H. A. Mook, and F. Dogan, *Phys. Rev. B* **54**, R6905 (1996).
- [13] H. F. Fong, P. Bourges, Y. Sidis, L. P. Regnault, A. Ivanov, G. D. Gu, N. Koshizuka, and B. Keimer, *Nature (London)* **398**, 588 (1999).
- [14] H. He, Y. Sidis, P. Bourges, G. D. Gu, A. Ivanov, N. Koshizuka, B. Liang, C. T. Lin, L. P. Regnault, E. Schoenher, and B. Keimer, *Phys. Rev. Lett.* **86**, 1610 (2001).
- [15] H. He, P. Bourges, Y. Sidis, C. Ulrich, L. P. Regnault, S. Pailh s, N. S. Berzigiarova, N. N. Kolesnikov, and B. Keimer, *Science* **295**, 1045 (2002).
- [16] B. Keimer, N. Belk, R. J. Birgeneau, A. Cassanho, C. Y. Chen, M. Greven, M. A. Kastner, A. Aharony, Y. Endoh, R. W. Erwin, and G. Shirane, *Phys. Rev. B* **46**, 14034 (1992).
- [17] S. Wakimoto, H. Zhang, K. Yamada, I. Swainson, H. Kim, and R. J. Birgeneau, *Phys. Rev. Lett.* **92**, 217004 (2004).
- [18] J. E. Sonier, C. V. Kaiser, V. Pacradouni, S. A. Sabok-Sayr, C. Cochran, D. E. MacLaughlin, S. Komiya, and N. E. Hussey, *Proc. Natl. Acad. Sci. USA* **107**, 17131 (2010).
- [19] S. Wakimoto, R. J. Birgeneau, A. Kagedan, H. Kim, I. Swainson, K. Yamada, and H. Zhang, *Phys. Rev. B* **72**, 064521 (2005).
- [20] V. Hinkov, P. Bourges, S. Pailh s, Y. Sidis, A. Ivanov, C. D. Frost, T. G. Perring, C. T. Lin, D. P. Chen, and B. Keimer, *Nat. Phys.* **3**, 780 (2007).
- [21] D. Meyers, H. Miao, A. C. Walters, V. Bisogni, R. S. Springell, M. d'Astuto, M. Dantz, J. Pellicciari, H. Y. Huang, J. Okamoto, D. J. Huang, J. P. Hill, X. He, I. Bozovic, T. Schmitt, and M. P. M. Dean, *Phys. Rev. B* **95**, 075139 (2017).
- [22] C. J. Jia, A. Nowadnick, K. Wohlfeld, Y. F. Kung, C.-C. Chen, S. Johnston, T. Tohyama, B. Moritz, and T. P. Devereaux, *Nat. Commun.* **5**, 3314 (2014).
- [23] M. Le Tacon, G. Ghiringhelli, J. Chaloupka, M. Moretti Sala, V. Hinkov, M. W. Haverkort, M. Minola, M. Bakr, K. J. Zhou, S. Blanco-Canosa, C. Monney, Y. T. Song, G. L. Sun, C. T. Lin, G. M. De Luca, M. Salluzzo, G. Khaliullin, T. Schmitt, L. Braicovich, and B. Keimer, *Nat. Phys.* **7**, 725 (2011).
- [24] M. Le Tacon, M. Minola, D. C. Peets, M. Moretti Sala, S. Blanco-Canosa, V. Hinkov, R. Liang, D. A. Bonn, W. N. Hardy, C. T. Lin, T. Schmitt, L. Braicovich, G. Ghiringhelli, and B. Keimer, *Phys. Rev. B* **88**, 020501(R) (2013).
- [25] M. P. M. Dean, G. Dellea, R. S. Springell, F. Yakhov-Harris, K. Kummer, N. B. Brookes, X. Liu, Y.-J. Sun, J. Strle, T. Schmitt, L. Braicovich, G. Ghiringhelli, I. Bozovic, and J. P. Hill, *Nat. Mater.* **12**, 1019 (2013).
- [26] S. Wakimoto, K. Yamada, J. M. Tranquada, C. D. Frost, R. J. Birgeneau, and H. Zhang, *Phys. Rev. Lett.* **98**, 247003 (2007).
- [27] G.-Q. Zheng, T. Kuse, Y. Kitaoka, K. Ishida, S. Ohsugi, K. Asayama, and Y. Yamada, *Physica C* **208**, 339 (1993).
- [28] S. Ohsugi, Y. Kitaoka, K. Ishida, G.-Q. Zheng, and K. Asayama, *J. Phys. Soc. Jpn.* **63**, 700 (1994).
- [29] K. Asayama, Y. Kitaoka, G.-Q. Zheng, K. Ishida, and S. Ohsugi, *Hyp. Int.* **79**, 835 (1993).
- [30] Y. Kitaoka, K. Fujiwara, K. Ishida, K. Asayama, Y. Shimakawa, T. Manako, and Y. Kubo, *Physica C* **179**, 107 (1991).
- [31] K. Ishida, Y. Kitaoka, K. Asayama, K. Kadowaki, and T. Mochiku, *J. Phys. Soc. Jpn.* **63**, 1104 (1994).
- [32] W. W. Warren, R. E. Walstedt, G. F. Brennert, R. J. Cava, R. Tycko, R. F. Bell, and G. Dabbagh, *Phys. Rev. Lett.* **62**, 1193 (1989).
- [33] M. Takigawa, A. P. Reyes, P. C. Hammel, J. D. Thompson, R. H. Heffner, Z. Fisk, and K. C. Ott, *Phys. Rev. B* **43**, 247 (1991).
- [34] K. Asayama, Y. Kitaoka, G.-Q. Zheng, and K. Ishida, *Prog. Nucl. Magn. Reson. Spectrosc.* **28**, 221 (1996).
- [35] C. Berthier, M. H. Julien, M. Horvatic, and Y. Berthier, *J. Phys. I France* **6**, 2205 (1996).

- [36] A. Rigamonti, F. Borsa, and P. Carretta, *Rep. Prog. Phys.* **61**, 1367 (1998).
- [37] H. Alloul, T. Ohno, and P. Mendels, *Phys. Rev. Lett.* **63**, 1700 (1989).
- [38] H. Alloul, A. Mahajan, H. Casalta, and O. Klein, *Phys. Rev. Lett.* **70**, 1171 (1993).
- [39] T. Auler, M. Horvatić, J. A. Gillet, C. Berthier, Y. Berthier, P. Ségransan, and J. Y. Henry, *Phys. Rev. B* **56**, 11294 (1997).
- [40] K. Fujiwara, Y. Kitaoka, K. Asayama, Y. Shimakawa, T. Manako, and Y. Kubo, *J. Phys. Soc.* **59**, 3459 (1990).
- [41] K. Fujiwara, Y. Kitaoka, K. Ishida, and K. Asayama, *Physica C* **184**, 207 (1991).
- [42] T. Imai, C. P. Slichter, K. Yoshimura, and K. Kosuge, *Phys. Rev. Lett.* **70**, 1002 (1993).
- [43] J. Haase, C. P. Slichter, and G. V. M. Williams, *J. Phys.: Condens. Matter* **21**, 455702 (2009).
- [44] M. Jurkutat, M. Avramovska, G. V. M. Williams, D. Dernbach, D. Pavicevic, and J. Haase, *J. Supercond. Novel Magn.* **32**, 3369 (2019).
- [45] N. J. Curro, T. Imai, C. P. Slichter, and B. Dabrowski, *Phys. Rev. B* **56**, 877 (1997).
- [46] M. K. Chan, C. J. Dorow, L. Mangin-Thro, Y. Tang, Y. Ge, M. J. Veit, G. Yu, X. Zhao, A. D. Christianson, J. T. Park, Y. Sidis, P. Steffens, D. L. Abernathy, P. Bourges, and M. Greven, *Nat. Commun.* **7**, 10819 (2016).
- [47] J. B. Torrance, A. Bezing, A. I. Nazzari, T. C. Huang, S. S. P. Parkin, D. T. Keane, S. J. LaPlaca, P. M. Horn, and G. A. Held, *Phys. Rev. B* **40**, 8872 (1989).
- [48] T. Nakano, M. Oda, C. Manabe, N. Momono, Y. Miura, and M. Ido, *Phys. Rev. B* **49**, 16000 (1994).
- [49] D. C. Johnston, *Phys. Rev. Lett.* **62**, 957 (1989).
- [50] N. Bulut, D. W. Hone, D. J. Scalapino, and N. E. Bickers, *Phys. Rev. B* **41**, 1797 (1990).
- [51] F. Mila and T. M. Rice, *Physica C* **157**, 561 (1989).
- [52] A. J. Millis, H. Monien, and D. Pines, *Phys. Rev. B* **42**, 167 (1990).
- [53] E. Pavarini, O. Jepsen, and O. K. Andersen, *Physica B* **312**, 39 (2002).
- [54] X. Wan, T. A. Maier, and S. Y. Savrasov, *Phys. Rev. B* **79**, 155114 (2009).
- [55] F. Mila, *Phys. Rev. B* **38**, 11358 (1988).
- [56] Y. Zha, V. Barzykin, and D. Pines, *Phys. Rev. B* **54**, 7561 (1996).
- [57] P. Monthoux and D. Pines, *Phys. Rev. B* **47**, 6069 (1993).
- [58] S. Renold, S. Plibersek, E. P. Stoll, T. A. Claxton, and P. F. Meier, *Eur. Phys. J. B* **23**, 3 (2001).
- [59] R. E. Walstedt, T. E. Mason, G. Aeppli, S. M. Hayden, and H. A. Mook, *Phys. Rev. B* **84**, 024530 (2011).
- [60] M. Randeria, N. Trivedi, A. Moreo, and R. T. Scalettar, *Phys. Rev. Lett.* **69**, 2001 (1992).
- [61] K.-S. Chen, Z. Y. Meng, S.-X. Yang, T. Pruschke, J. Moreno, and M. Jarrell, *Phys. Rev. B* **88**, 245110 (2013).
- [62] E. Pavarini, I. Dasgupta, T. Saha-Dasgupta, O. Jepsen, and O. K. Andersen, *Phys. Rev. Lett.* **87**, 047003 (2001).
- [63] E. Pavarini, I. Dasgupta, T. Saha-Dasgupta, and O. K. Andersen, *Phys. Rev. Lett.* **124**, 109701 (2020).
- [64] T. A. Maier, M. Jarrell, T. Pruschke, and M. Hettler, *Rev. Mod. Phys.* **77**, 1027 (2005).
- [65] Y. F. Kung, E. A. Nowadnick, C. J. Jia, S. Johnston, B. Moritz, R. T. Scalettar, and T. P. Devereaux, *Phys. Rev. B* **92**, 195108 (2015).
- [66] X. Chen, J. P. F. LeBlanc, and E. Gull, *Nat. Commun.* **8**, 14986 (2017).
- [67] J. P. F. LeBlanc, S. Li, X. Chen, R. Levy, A. E. Antipov, A. J. Millis, and E. Gull, *Phys. Rev. B* **100**, 075123 (2019).
- [68] E. A. Stepanov, L. Peters, I. S. Krivenko, A. I. Lichtenstein, M. I. Katsnelson, and A. N. Rubtsov, *npj Quant. Mater.* **3**, 54 (2018).
- [69] A. Kopp, A. Ghosal, and S. Chakravarty, *Proc. Natl. Acad. Sci. USA* **104**, 6123 (2007).
- [70] R. Eder, *Phys. Rev. B* **100**, 085133 (2019).
- [71] B.-X. Zheng, C.-M. Chung, P. Corboz, G. Ehlers, M.-P. Qin, R. M. Noak, H. Shi, S. R. White, S. Zhang, and G. K.-L. Chan, *Science* **358**, 1115 (2017).
- [72] M.-P. Qin, C.-M. Chung, H. Shi, E. Vitali, C. Hubig, U. Schollwöck, S. R. White, and S. Zhang, *Phys. Rev. X* **10**, 031016 (2020).
- [73] U. Kumar, A. Nocera, G. Price, K. Stiwwinter, S. Johnston, and T. Datta, *Phys. Rev. B* **102**, 075134 (2020).
- [74] H. C. Jiang and T. P. Devereaux, *Science* **365**, 1424 (2019).
- [75] Y. F. Jiang, J. Zaanen, T. P. Devereaux, and H.-C. Jiang, *Phys. Rev. Res.* **2**, 033073 (2020).
- [76] E. W. Huang, C. B. Mendl, H.-C. Jiang, B. Moritz, and T. P. Devereaux, *npj Quantum Mater.* **3**, 22 (2018).
- [77] H. Park, K. Haule, C. A. Marianetti, and G. Kotliar, *Phys. Rev. B* **77**, 035107 (2008).
- [78] H. Park, K. Haule, and G. Kotliar, *Phys. Rev. Lett.* **101**, 186403 (2008).
- [79] K. Kurashima, T. Adachi, K. M. Suzuki, Y. Fukunaga, T. Kawamata, T. Noji, H. Miyasaka, I. Watanabe, M. Miyazaki, A. Koda, R. Kadono, and Y. Koike, *Phys. Rev. Lett.* **121**, 057002 (2018).
- [80] P. Werner, X. Chen, and E. Gull, *Phys. Rev. Res.* **2**, 023037 (2020).
- [81] P. Werner, S. Hoshino, and H. Shinaoka, *Phys. Rev. B* **94**, 245134 (2016).
- [82] A. H. MacDonald, S. M. Girvin, and D. Yoshioka, *Phys. Rev. B* **37**, 9753 (1988).
- [83] M. Roger and J. M. Delrieu, *Phys. Rev. B* **39**, 2299 (1989).
- [84] P. Werner, R. Sakuma, F. Nilsson, and F. Aryasetiawan, *Phys. Rev. B* **91**, 125142 (2015).
- [85] S. W. Jang, H. Sakakibara, H. Kino, T. Kotani, K. Kuroki, and M. J. Han, *Sci. Rep.* **6**, 33397 (2016).
- [86] A. K. McMahan, R. M. Martin, and S. Satpathy, *Phys. Rev. B* **38**, 6650 (1988).
- [87] M. S. Hybertsen, M. Schlüter, and N. E. Christensen, *Phys. Rev. B* **39**, 9028 (1989).
- [88] V. I. Anisimov, M. A. Korotin, I. A. Nekrasov, Z. V. Pchelkina, and S. Sorella, *Phys. Rev. B* **66**, 100502(R) (2002).
- [89] F. Aryasetiawan, K. Karlsson, O. Jepsen, and U. Schönberger, *Phys. Rev. B* **74**, 125106 (2006).
- [90] A. Georges, G. Kotliar, W. Krauth, and M. J. Rozenberg, *Rev. Mod. Phys.* **68**, 13 (1996).
- [91] E. Pavarini, E. Koch, D. Vollhardt, and A. I. Lichtenstein, editors, *The LDA+DMFT Approach to Strongly Correlated Materials*, Modeling and Simulation, Vol. 1 (Verlag des Forschungszentrum Jülich, Jülich, 2011). Open access at

- <http://www.cond-mat.de/events/correl.html> and <http://hdl.handle.net/2128/4467>.
- [92] E. Pavarini, E. Koch, D. Vollhardt, and A. I. Lichtenstein, editors, *DMFT at 25: Infinite Dimensions*, Modeling and Simulation, Vol. 4 (Verlag des Forschungszentrum Jülich, Jülich, 2014). Open access at <http://www.cond-mat.de/events/correl.html> and <http://hdl.handle.net/2128/7937>.
- [93] N. Nucker, J. Fink, B. Renker, D. Ewert, C. Politis, P. J. W. Weijs, and J. C. Fuggle, *Z. Phys. B*, **67**, 9 (1987).
- [94] J. M. Ginder, M. G. Roe, Y. Song, R. P. McCall, J. R. Gaines, E. Ehrenfreund, and A. J. Epstein, *Phys. Rev. B* **37**, 7506 (1988).
- [95] S. Uchida, T. Ido, H. Takagi, T. Arima, Y. Tokura, and S. Tajima, *Phys. Rev. B* **43**, 7942 (1991); D. N. Basov and T. Timusk, *Rev. Mod. Phys.* **77**, 721 (2005).
- [96] M. Merz, N. Nücker, P. Schweiss, S. Schuppler, C. T. Chen, V. Chakarian, J. Freeland, Y. U. Idzerda, M. Kläser, G. Müller-Vogt, and Th. Wolf, *Phys. Rev. Lett.* **80**, 5192 (1998).
- [97] DMFT, as is well known, overestimates T_N due to the mean-field approximation [64] and for a strictly two-dimensional system $T_N \rightarrow 0$ in the infinite-cluster limit (Mermin-Wagner theorem). The correct T_N is however not relevant to the discussion presented here; the values are used to study the trends in the magnetic correlation strengths.
- [98] K. Haule and G. Kotliar, *Phys. Rev. B* **76**, 104509 (2007).
- [99] J. E. Hirsch and R. M. Fye, *Phys. Rev. Lett.* **56**, 2521 (1986).
- [100] A. Kiani and E. Pavarini, *Phys. Rev. B* **94**, 075112 (2016).
- [101] P. Werner, A. Comanac, L. de' Medici, M. Troyer, and A. J. Millis, *Phys. Rev. Lett.* **97**, 076405 (2006).
- [102] A. Flesch, E. Gorelov, E. Koch, and E. Pavarini, *Phys. Rev. B* **87**, 195141 (2013).
- [103] J. Musshoff, G. Zhang, E. Koch, and E. Pavarini, *Phys. Rev. B* **100**, 045116 (2019).
- [104] M. Jarrell, *Phys. Rev. Lett.* **69**, 168 (1992).
- [105] T. Thio and A. Aharony, *Phys. Rev. Lett.* **73**, 894 (1994).
- [106] P. E. Sulewski, P. A. Fleury, K. B. Lyons, S-W. Cheong, and Z. Fisk, *Phys. Rev. B* **41**, 225 (1990).
- [107] K. B. Lyons, P. A. Fleury, L. F. Schneemeyer, and J. V. Waszczak, *Phys. Rev. Lett.* **60**, 732 (1988).
- [108] M. Ogata and H. Fukuyama, *Rep. Prog. Phys.* **71**, 036501 (2008).
- [109] K. B. Lyons, P. A. Fleury, J. P. Remeika, A. S. Cooper, and T. J. Negran, *Phys. Rev. B* **37**, 2353 (1988).
- [110] M. Greger, M. Kollar, and D. Vollhardt, *Phys. Rev. B* **87**, 195140 (2013).
- [111] J. Haase, D. Rybicki, C. P. Slichter, M. Greven, G. Yu, Y. Li, and X. Zhao, *Phys. Rev. B* **85**, 104517 (2012).
- [112] T. Moriya, *Prog. Theor. Phys.* **28**, 371 (1962).
- [113] M. Jarrell and Th. Pruschke, *Phys. Rev. B* **49**, 1458 (1994).
- [114] W.-J. Li, C.-J. Lin, and T.-K. Lee, *Phys. Rev. B* **94**, 075127 (2016).
- [115] C. Jia, K. Wohlfeld, Y. Wang, B. Moritz, and T. P. Devereaux, *Phys. Rev. X* **6**, 021020 (2016).
- [116] www.gauss-centre.eu.
- [117] M. Maška, *Phys. Rev. B* **48**, 1160 (1993).
- [118] M. Potthoff, T. Herrmann, T. Wegner, and W. Nolting, *Phys. Status Solidi B* **210**, 199 (1998).